Cell

A type 1 immune-stromal cell network mediates disease tolerance against intestinal infection

Graphical abstract

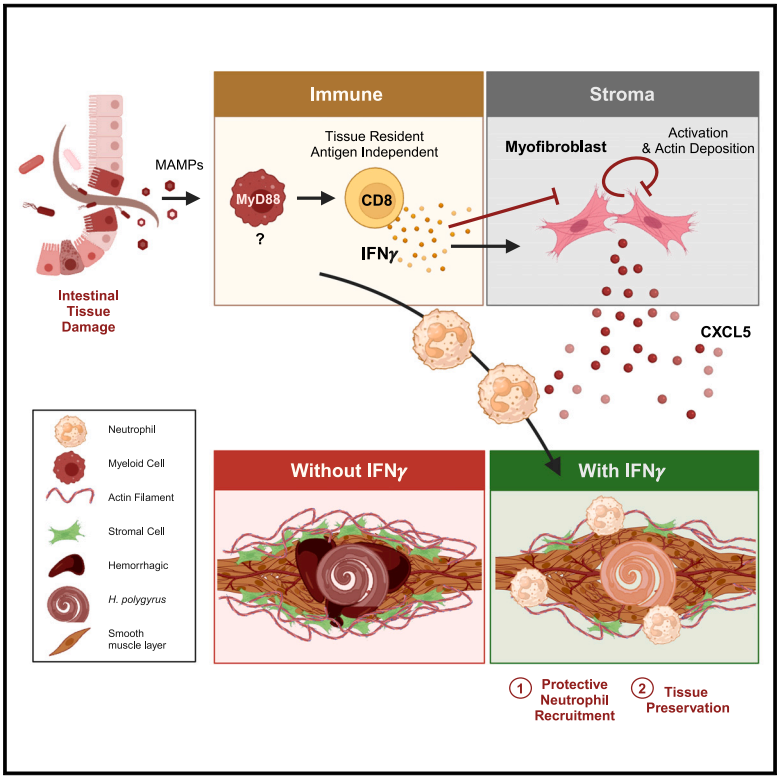

Highlights

- Type 1 immunity is required for disease tolerance to tissue-invasive infection
- Microbiota drive gut-resident CD8$^+$ T cells to produce IFNγ, independent of antigen
- IFNγ signaling recruits neutrophils to limit helminth-induced tissue injury
- Stromal sensing of IFNγ limits tissue dysfunction and gut dysmotility during infection

Authors

Susan Westfall, Maria E. Gentile, Tayla M. Olsen, ..., Sebastian Weis, Alex Gregorieff, Irah L. King

Correspondence

irah.king@mcgill.ca

In brief

The significant tissue damage imposed by intestinal helminths is controlled by a type 1 immune response. Triggered by the microbiota, gut-resident CD8$^+$ T cells release IFNγ to preserve organ function and host survival through stromal cell-specific signaling and recruitment of tissue-protective neutrophils.

Westfall et al., 2025, Cell *188*, 3135–3151
June 12, 2025
https://doi.org/10.1016/j.cell.2025.03.043

CellPress

Cell

CellPress

Article

A type 1 immune-stromal cell network mediates disease tolerance against intestinal infection

Susan Westfall,[1,2] Maria E. Gentile,[1,3] Tayla M. Olsen,[4] Danielle Karo-Atar,[5] Andrei Bogza,[1,2] Franziska Röstel,[6,7] Ryan D. Pardy,[8] Giordano Mandato,[1,2] Ghislaine Fontes,[1,2] De'Broski Herbert,[3] Heather J. Melichar,[9] Valerie Abadie,[10] Martin J. Richer,[9,11] Donald C. Vinh,[1] Joshua F.E. Koenig,[12] Oliver J. Harrison,[4] Maziar Divangahi,[1] Sebastian Weis,[6,7,13] Alex Gregorieff,[14,15] and Irah L. King[1,2,15,16,17,*]

[1]Department of Microbiology and Immunology, Department of Medicine, Meakins-Christie Laboratories, Research Institute of McGill University Health Centre, Montreal, QC, Canada
[2]McGill Centre for Microbiome Research, Montreal, QC, Canada
[3]Department of Pathobiology, School of Veterinary Medicine, University of Pennsylvania, Philadelphia, PA, USA
[4]Center for Fundamental Immunology, Benaroya Research Institute, Seattle, WA, USA
[5]Department of Clinical Biochemistry and Pharmacology, Ben Gurion University of the Negev, Beer-Sheva, Israel
[6]Institute for Infectious Disease and Infection Control, Jena University Hospital, Friedrich-Schiller-University, Jena, Germany
[7]Leibniz Institute for Natural Product Research and Infection Biology, Jena, Germany
[8]Institut National de la Recherche Scientifique, Centre Armand-Frappier, Laval, QC, Canada
[9]Department of Microbiology and Immunology, McGill University Montreal, Montreal, QC, Canada
[10]Committee on Immunology, University of Chicago, Chicago, IL, USA
[11]Department of Microbiology and Immunology, Indiana University School of Medicine, Indianapolis, IN, USA
[12]Department of Medicine, Faculty of Health Sciences, McMaster University, Hamilton, ON, Canada
[13]Department of Anesthesiology and Intensive Care Medicine, Jena University Hospital, Friedrich-Schiller-University, Jena, Germany
[14]Department of Pathology, McGill University and Cancer Research Program, Research Institute of McGill University Health Centre, Montreal, QC, Canada
[15]McGill Regenerative Medicine Network, Montreal, QC, Canada
[16]McGill Interdisciplinary Initiative in Infection and Immunity, Montreal, QC, Canada
[17]Lead contact
*Correspondence: irah.king@mcgill.ca
https://doi.org/10.1016/j.cell.2025.03.043

SUMMARY

Type 1 immunity mediates host defense through pathogen elimination, but whether this pathway also impacts tissue function is unknown. Here, we demonstrate that rapid induction of interferon γ (IFNγ) signaling coordinates a multicellular response that is critical to limit tissue damage and maintain gut motility following infection of mice with a tissue-invasive helminth. IFNγ production is initiated by antigen-independent activation of lamina propria $CD8^+$ T cells following MyD88-dependent recognition of the microbiota during helminth-induced barrier invasion. IFNγ acted directly on intestinal stromal cells to recruit neutrophils that limited parasite-induced tissue injury. IFNγ sensing also limited the expansion of smooth muscle actin-expressing cells to prevent pathological gut dysmotility. Importantly, this tissue-protective response did not impact parasite burden, indicating that IFNγ supports a disease tolerance defense strategy. Our results have important implications for managing the pathophysiological sequelae of post-infectious gut dysfunction and chronic inflammatory diseases associated with stromal remodeling.

INTRODUCTION

Decades of research have made incredible advances in our understanding of host resistance, that is, pathogen elimination. However, our knowledge of pathways that limit tissue damage to ensure survival in the face of persistent infection, a host defense strategy referred to as disease tolerance, is comparatively limited.[1] A relevant, yet understudied, setting to investigate the mechanisms of disease tolerance is intestinal helminth infection.[2] Helminths are large, tissue-invasive parasites that migrate through host tissues to complete their life cycle, resulting in profound tissue damage. Remarkably, however, most enteric helminths colonize their hosts without inducing overt morbidity, likely contributing to their pervasiveness across mammalian species.[3]

Compared with microbial pathogens such as bacteria, viruses, and fungi, the size and tissue-invasive nature of helminths pose unique challenges to their hosts. As a result, type 2 immune responses, including the production of interleukin (IL)-4 and IL-13, evolved to promote the expulsion of diverse enteric helminth

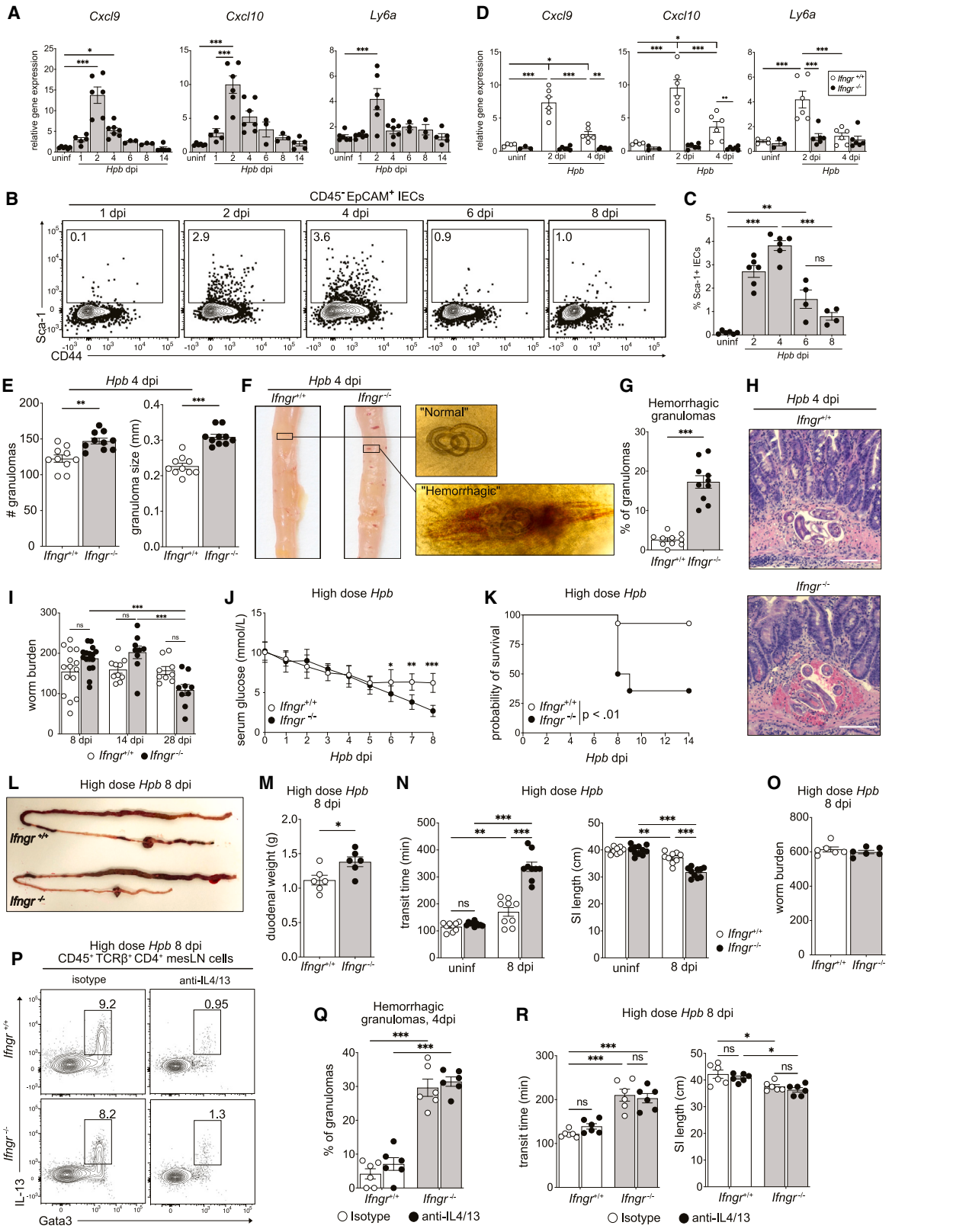

(legend on next page)

species by enhancing the physiological functions of the intestine, including motility, epithelial turnover, and mucus secretion.[4] Tissue-specific type 2 cytokine signaling also induces *de novo* generation of reparative monocytes/macrophages that execute wound healing.[5] However, the "weep and sweep" and tissue repair functions of type 2 immunity are dominant during the luminal stage of helminth infection, leaving unanswered questions about the host defense pathways that limit tissue damage imposed during the invasive stage of infection.

We and others have described a transient, yet robust, type 1 immune response during the tissue-invasive stage of infection with *Heligmosomoides polygyrus bakeri* (*Hpb*), an enteric parasitic roundworm.[6–8] This response is characterized by interferon γ (IFNγ)-dependent transcription of interferon-stimulated genes (ISGs) that largely precedes the canonical type 2 immune response.[6] Although classically involved in microbe elimination and anti-tumor immunity,[9] ISG expression during *Hpb* infection has been suggested to promote regeneration of the gut barrier by inducing Sca-1$^+$ fetal-like intestinal epithelial cells (IECs).[7] In addition, direct IFNγ signaling on enteric glial cells acts to repair *Hpb*-induced granulomatous lesions.[8] IFNγ signaling also preserves barrier integrity by recruiting tissue-protective natural killer (NK) cells to the *Hpb* infection site.[6] These effects were independent of changes in parasite burden, suggesting that, in this context, type 1 immunity may be integral to disease tolerance.[1,10]

Here, we performed an in-depth analysis of the cellular sources and targets of IFNγ signaling to reveal the fundamental type 1 immune networks required to endure an enteric helminth infection. We demonstrate that a breach of the epithelial barrier elicits microbiota-dependent activation of tissue-resident lamina propria CD8$^+$ T cells that rapidly produce IFNγ in an antigen-independent manner. Despite widespread IFNγ signaling at the site of infection, direct sensing of this cytokine by the small intestinal stromal cell compartment is critical for the recruitment of tissue-protective neutrophils and restraining the expansion of smooth muscle actin-expressing cells. Indeed, germline or stromal cell-specific deletion of the IFNγ receptor resulted in enhanced granulomatous pathology and, following high-dose parasite challenge, severe gut dysmotility and mortality. Collectively, this study reveals the unexpected functions of IFNγ in disease tolerance and provides a conceptual framework for investigating how immune pathways, conventionally thought to only mediate host resistance, ensure tissue preservation during infection.

RESULTS

Type 1 immune activation during early *Hpb* infection controls parasite-induced tissue damage and preserves organ function

We and others have previously shown that IFNγ activity dominates the intestinal immune landscape during the tissue-invasive phase of *Hpb* infection.[6,7] To further evaluate the dynamics of IFNγ signaling, we performed a kinetic analysis of ISG expression during the tissue-invasive (days 1–6) and luminal stages (days 8–14) of *Hpb* infection. We found ISG expression to be robust yet transient with *Cxcl9, Cxcl10,* and *Ly6a* (encoding for Sca-1) mRNA all highly expressed at 2 days post-infection (dpi) and rapidly decreasing thereafter (Figure 1A). Similarly, surface Sca-1 expression by IECs also peaked between 2–4 dpi (Figures 1B and 1C). This response was specific to IFNγ signaling because *Hpb*-infected mice with a germline deletion of the IFNγ receptor (*Ifngr*$^{-/-}$) failed to induce ISGs at these time points compared with IFNγR-sufficient (*Ifngr*$^{+/+}$) animals (Figure 1D).

We next assessed gross changes to the larval-induced granulomas in IFNγR-sufficient and -deficient mice. At 4 dpi, we observed an increase in the number and size of detectable granulomas in *Ifngr*$^{-/-}$ mice compared with controls (Figure 1E). We also found an increased frequency of granulomatous lesions in the *Ifngr*$^{-/-}$ mice (Figures 1F and 1G), which were confirmed to be hemorrhagic by a positive blood stain with intense eosin Y signal (Figure 1H) as well as detection of intravenously administered tetramethylrhodamine isothiocyanate (TRITC)-Dextran dye in the granulomas of Ifngr$^{-/-}$, but not control, mice (Figure S1A).

Figure 1. Transient IFNγ signaling limits tissue damage and mediates disease tolerance during tissue-invasive helminth infection

(A–C) Kinetic analysis of (A) interferon-stimulated genes (ISGs) from small intestinal tissue at the indicated time points after *Hpb* infection (dpi, days post-infection). (B) Representative contour plots of Sca-1 by small intestinal epithelial cells (IECs) gated on viable CD45$^-$EpCAM$^+$ cells quantified in (C) as a percentage of Sca-1$^+$ IECs.

(D) Small intestinal ISG expression from *Ifngr*$^{+/+}$ and *Ifngr*$^{-/-}$ mice.

(E) Enumeration of total visible granulomas (left) and their diameter (right) at 4 dpi. Each data point represents an average of 30 granulomas per mouse.

(F) Representative images of the duodenum at 4 dpi with an inset of normal and "hemorrhagic" granulomas.

(G) Frequency of hemorrhagic granulomas. Three independent experiments, $n = 10$ per group.

(H) Representative H&E images of *Hpb* granulomas at 4 dpi. Scale bar, 50 μm.

(I) Worm burden following infection with 200L3 *Hpb* larvae. Four independent experiments, $n = 9–16$ per group.

(J) Daily unfasted blood glucose levels from high-dose infected mice (600L3 larvae), $n = 16$ per group.

(K) Kaplan-Meier survival curve of high-dose *Hpb*-infected mice, three independent experiments, $n = 14$ per group.

(L and M) (L) Representative image at day 8 post-high-dose infection with (M) quantification of duodenal weight.

(N) Transit time (left) and small intestinal (SI) length (right).

(O) Worm burden at 8 dpi following high-dose infection.

(P) Representative contour plots of mesenteric lymph node (mesLN) IL-13$^+$ Gata3$^+$ CD4 T cells at 8 days post-high-dose infection +/− anti-IL-4 and anti-IL-13.

(Q and R) (Q) Frequency of hemorrhagic granulomas at 4 dpi following 200L3 challenge and (R) transit time (left) and SI length (right) at 8 dpi with 600 L3 larvae +/− anti-IL-4 and anti-IL-13 treatment. Two to three independent experiments, $n = 5–10$ mice per group unless otherwise noted. Each dot represents an individual mouse. Between-group comparisons were analyzed with nonparametric Student's t test and time course analyses with two-way ANOVA and Tukey's post hoc analysis. $^*p < 0.05$, $^{**}p < 0.01$, $^{***}p < 0.001$; ns, not significant. Survival curves were analyzed using log-rank (Mantel-Cox) test.

See also Figures S1 and S2.

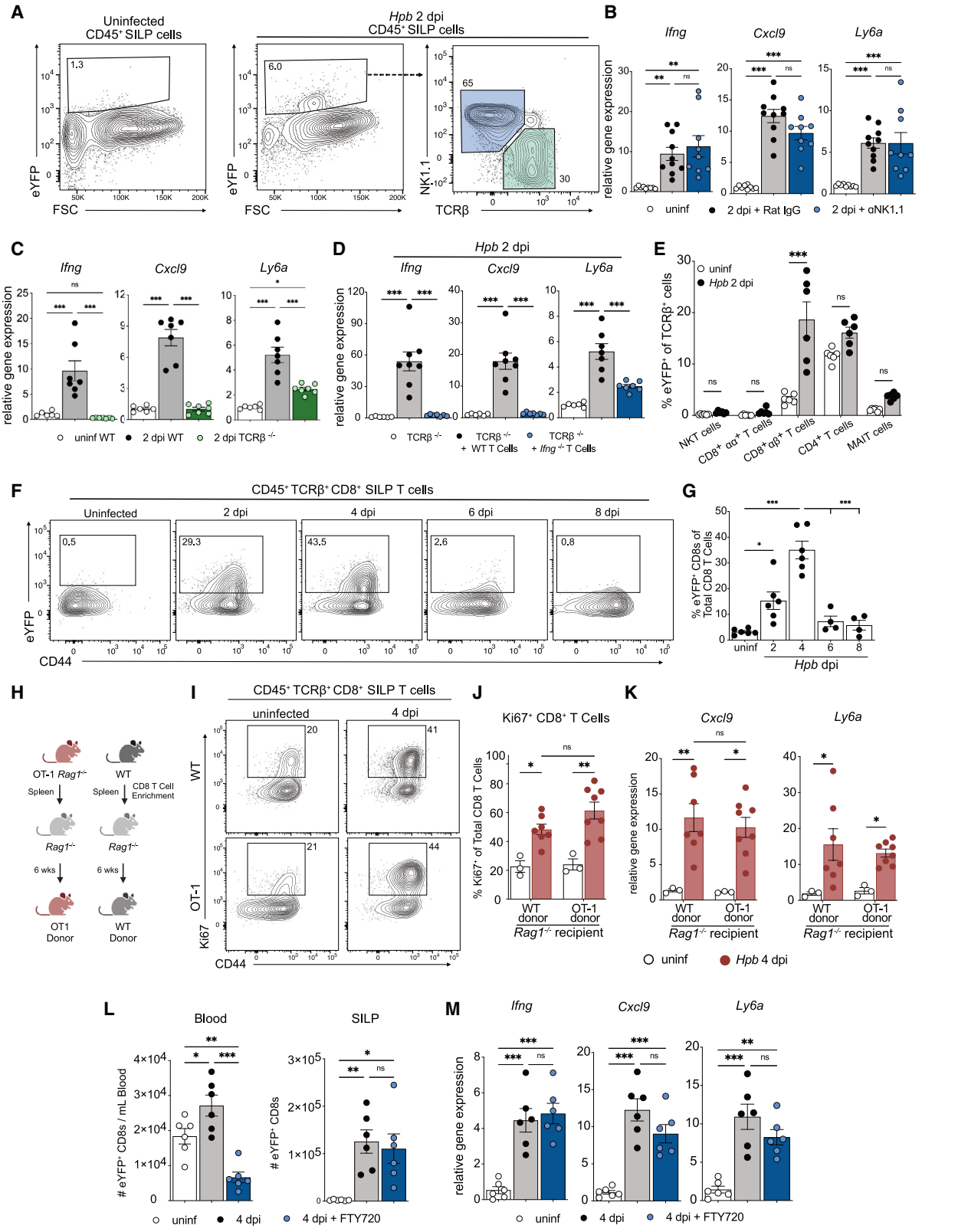

(legend on next page)

Blinded granuloma examination provided similar results (Figure S1B). Conversely, treatment of Ifngr$^{+/+}$ mice with low-dose recombinant IFNγ decreased the number and size of visible granulomas (Figure S1C), further indicating that type 1 cytokine signaling reduces helminth-induced tissue remodeling. We did not detect differences in barrier permeability as quantified by serum fluorescein isothiocyanate (FITC)-dextran following gavage (Figure S1D) or differences in circulating endotoxin levels (Figure S1E). Importantly, there was no difference in the number of adult *Hpb* worms between groups at 8 dpi, the earliest time point in which adult parasites can be detected in the intestinal lumen[11] (Figure 1I). However, we did detect a decrease in adult worms isolated from the intestine of *Ifngr*$^{-/-}$ mice compared with controls at later time points of infection, a finding consistent with a previous study[12] (Figure 1I). These results indicate that transient activation of IFNγ signals restrains helminth-induced damage during the tissue-invasive stage of infection, independent of parasite burden.

Although we observed an increase in tissue damage in the absence of IFNγ signals using a conventional infection dose (200 L3 larvae), no appreciable sickness behavior (e.g., weight loss or altered posturing) was noted. To test whether a higher dose of *Hpb* would exacerbate the phenotype we observed at day 4 and result in disease manifestation, we challenged mice with 600 L3 larvae. *Ifngr*$^{-/-}$ mice exhibited a greater reduction in systemic glucose levels and a 75% mortality rate compared with *Ifngr*$^{+/+}$ mice (Figures 1J and 1K). While we detected a larger increase in serum endotoxin levels in the *Ifngr*$^{-/-}$ mice compared with controls (Figure S1F), sepsis did not appear to be a key driver of mortality as no striking differences in systemic bacterial translocation or serological indicators of organ failure were apparent (Figures S1G and S1H). Similarly, serum cytokine quantification was similar between groups, except for an increase in IFNγ and smaller increases in IL-17 and IL-6 in high-dose infected *Ifngr*$^{-/-}$ mice (Figure S1I). Furthermore, we could not detect a difference in food intake or weight loss (Figures S1J and S1K). Rather, digestive contents aggregated in the small intestinal lumen of *Ifngr*$^{-/-}$ mice (Figure 1L), where *Hpb* infection primarily takes place, resulting in an overall increase in intestinal weight of this region (Figure 1M). High-dose *Hpb* infection also induced a significant increase in intestinal transit time in *Ifngr*$^{+/+}$ and *Ifngr*$^{-/-}$ mice at 8 dpi compared with uninfected animals (Figure 1N). Differences in transit time were coupled with a significant shortening of the infected small intestine that was also greater in *Ifngr*$^{-/-}$ mice compared with controls (Figure 1N), without differences in parasite burden (Figures 1O and S1L). Together, these results indicate that high-dose *Hpb* infection induces an altered physiological set point of intestinal function, an adaptation that cannot be achieved in the absence of IFNγ signals.

Since IFNγ signaling is antagonistic to canonical type 2 cytokine production,[13] we performed immunophenotyping of the small intestinal lamina propria (SILP) and gut-draining mesenteric lymph node (mesLN) cells at various time points after *Hpb* infection. Our results showed a significant increase in Gata3^{+}IL-13^{+} Th2 cells in the mesLN and SILP of *Hpb*-infected mice as early as 4 and 6 dpi, respectively, and as previously reported,[14] the magnitude of this response in *Ifngr*$^{-/-}$ mice was increased compared with *Ifngr*$^{+/+}$ mice (Figures S2A and S2B). We also observed a trending increase in type 2 innate lymphoid cells in the small intestine of *Ifngr*$^{-/-}$ mice compared with controls by 6 dpi (Figure S2C). Consistently, an enhanced type 2 immune gene signature and increased numbers of goblet and tuft cells were present in the small intestine of *Hpb*-infected *Ifngr*$^{-/-}$ mice compared with controls at 6–8 dpi (Figures S2D and S2E). To test whether type 2 cytokines contribute to pathophysiological changes in the absence of IFNγ signaling during *Hpb* infection, we neutralized IL-4 and IL-13 using function-blocking antibodies in *Ifngr*$^{+/+}$ and *Ifngr*$^{-/-}$ mice and assessed tissue pathology and dysfunction at 4 and 8 dpi with low and high-dose infection, respectively. Despite effective blockade of type 2 cytokine activity (as determined by prevention of Th2 cell differentiation; Figures 1P and S2F), we did not observe any granuloma differences at 4 dpi (Figures 1Q and S2G). In addition, blockade of IL-4 and IL-13 had no impact on intestinal length or transit time between groups after high-dose infection (Figure 1R). Collectively, these results indicate that transient IFNγ signaling promotes disease tolerance, independent of type 2 cytokine production and parasite load.

Antigen-independent production of IFNγ by tissue-resident CD8^{+} T cells drives the type 1 immune signature during *Hpb* infection

Diverse subsets of immune cells are capable of producing IFNγ during early *Hpb* infection.[7] Using IFNγ reporter mice in which *Ifng* mRNA is detectable by eYFP expression,[15] we found an increase in eYFP^{+} cells as early as day 2 post-infection and confirmed that more than 90% of these cells were either TCRβ^{+} αβ T cells or NK1.1^{+} TCRβ^{-} NK cells (Figure 2A). Depletion of NK cells during *Hpb* infection[6] did not impact ISG

Figure 2. Tissue-resident CD8^{+} T cells produce IFNγ independent of cognate antigen

(A–D) (A) Representative contour plots of total IFNγ^{+} (eYFP^{+}) cells from the small intestinal lamina propria (SILP) of uninfected and day 2 *Hpb*-infected mice, pre-gated on viable CD45^{+} cells. SILP ISG expression in (B) WT mice treated with control or anti-NK1.1, (C) WT or TCRβ$^{-/-}$ mice, or (D) TCRβ$^{-/-}$ mice following adoptive transfer of total WT or *Ifng*$^{-/-}$ T cells.

(E) Frequency of eYFP^{+} TCRβ^{+} T cell subsets at 2 dpi.

(F and G) (F) Representative contour plots of eYFP^{+} CD8 T cells during *Hpb* infection, gated on viable CD45^{+} TCRβ^{+} CD8^{+} SILP cells, quantified in (G).

(H) Schema of OT-1 adoptive transfer experiment.

(I) Representative contour plots of proliferating (Ki67^{+}) OT-1- or WT-derived CD8^{+} T cells at 4 dpi, pre-gated on CD45^{+} TCRβ^{+} CD8^{+} T cells.

(J and K) (J) Frequency of Ki67^{+} CD8^{+} T cells and (K) SILP ISG expression at 4 dpi.

(L and M) (L) Number of eYFP^{+} CD8^{+} T cells in blood (left) and SILP (right) of 4 dpi, FTY720-treated mice with (M) SILP ISG expression. Pooled results from 2–3 independent experiments with n = 6–10 mice per group. Between-group comparisons were analyzed with nonparametric Student's t tests, while time course analyses included one- or two-way ANOVAs with Tukey's post hoc analysis. *p < 0.05, **p < 0.01, and ***p < 0.001; ns, not significant.

See also Figures S2, S3, and S4.

induction (Figure 2B). By contrast, infection of TCRβ$^{-/-}$ mice abrogated ISG expression compared with wild-type (WT) controls (Figure 2C). To test whether IFNγ production by T cells was sufficient to induce ISG expression, TCRβ-deficient mice received WT or IFNγ$^{-/-}$ T cells and, 2 weeks later, were infected with *Hpb*. Notably, the transfer of WT, but not IFNγ-deficient, T cells restored ISG expression in TCRβ-deficient animals (Figure 2D). These data indicate that T cell-derived IFNγ is necessary and sufficient to drive intestinal ISG expression during *Hpb* infection. Using *Ifng*-eYFP expression to examine the T cell response to infection revealed that SILP CD8$^+$ αβ T cells significantly increased eYFP expression at the peak time of ISG expression (Figure 2E). eYFP$^+$ CD4$^+$ T cells were also detected, but their frequency did not differ between uninfected and infected conditions (Figure 2E). Mirroring the kinetics of ISG expression (Figure 1A), the frequency of eYFP$^+$ CD8$^+$ T cells peaked at 2 and 4 dpi (Figures 2F and 2G), which was not observed in CD4$^+$ T cells (Figure S2H). These results were further confirmed by *in vitro* phorbol myristate acetate (PMA)/ionomycin stimulation at the same time points in non-reporter mice (Figures S2I and S2J). As an additional approach, we acutely depleted CD4$^+$ T cells, CD8$^+$ T cells, or both during *Hpb* infection. Interestingly, single subset depletion only partially decreased intestinal ISG induction, compared with combined depletion (Figures S3A–S3C). Thus, while CD8$^+$ T cells are the responsive cell type in immune-replete conditions, CD4$^+$ T cells can compensate in their absence.

We next tested whether CD8$^+$ T cells were sufficient to induce IFNγ-dependent gene expression during *Hpb* infection. To this end, we used a previously published protocol[16] in which we transferred CD8$^+$ T cells from the spleens of C57BL/6 or OT-1 x Rag1$^{-/-}$ animals—in which the entire lymphocyte repertoire of the latter is ovalbumin-specific CD8$^+$ T cells—into Rag1$^{-/-}$ recipients 6 weeks prior to *Hpb* infection (Figure 2H). This combined approach also allowed us to test whether CD8$^+$ T cell activation during *Hpb* infection could occur in an antigen-independent manner. Consistent with prior results,[16] we readily detected donor T cells in the SILP of uninfected and infected recipients, which increased Ki67 expression following infection (Figures 2I and 2J). Remarkably, we observed an equal increase in ISG induction in both groups of recipients at 4 dpi (Figure 2K). Given the rapid induction of IFNγ-producing CD8$^+$ T cells during *Hpb* infection and that no *Hpb*-derived major histocompatibility complex class I (MHC class I)-restricted antigens have been described, this experiment suggests that SILP CD8$^+$ T cells were activated in an antigen-independent manner. Indeed, we observed similar activation of Thy1.1$^+$ lymphocytic choriomeningitis virus (LCMV)-specific P14 donor cells in C57BL/6 mice (hosting an endogenous T cell repertoire) previously infected with LCMV Armstrong and then challenged with *Hpb* 1 month later (Figures S3D–S3F). Together, these results indicate that CD8$^+$ αβ T cells are sufficient to drive IFNγ target gene expression in the intestine during *Hpb* infection in an antigen-independent manner.

We next examined whether eYFP$^+$ CD8$^+$ T cells were tissue-resident or derived from the circulation. Immunophenotyping indicated that eYFP$^+$ cells expressed a CD44$^+$CD62L$^-$ memory phenotype with variable expression of CD49d, CD103, CD69, PD-1, and ICOS (Figure S3G). Intravenous (i.v.) administration of a fluorochrome-conjugated anti-CD45 antibody at 4 dpi 3 mi before sacrifice demonstrated that eYFP$^+$ CD8$^+$ T cells found in the SILP cell preparation were not within the intestinal vasculature (Figures S4A–S4C). We could detect an increase in eYFP$^+$ CD8$^+$ T cells in mesLN, Peyer's patches, and, to a lesser degree, the bone marrow, but not until 4 dpi, a later time point than initial CD8$^+$ T cell activation in the SILP (Figure S4D). Consistently, expression of the gut-homing integrin α4β7 was not detectable in SILP CD8$^+$ T cells until day 4 (Figure S4E). To formally test whether CD8$^+$ tissue-resident memory (Trm) T cells were critical for ISG expression in the *Hpb*-infected intestine, we blocked migration of circulating T cells by administration of the sphingosine 1-phosphate receptor agonist FTY720[17] prior to and during infection. As expected, FTY720 treatment led to a significant decrease in the number of detectable eYFP$^+$ CD8$^+$ T cells in the circulation. However, FTY720 had no impact on the number of SILP eYFP$^+$ CD8$^+$ T cells or induction of ISG expression in the small intestine (Figures 2L and 2M).

IFNγ production during *Hpb* infection requires the gut microbiota and MyD88 signaling

To investigate the trigger of IFNγ production by CD8$^+$ Trm cells, we tested several antigen-independent modes of activation. IL-33 and IL-36γ, although upregulated at the transcriptional level during early *Hpb* infection (Figure S5A), were dispensable for IFNγ production from CD8$^+$ T cells *in vivo* and *in vitro* (Figures S5B–S5E). Likewise, *Il18* was upregulated during early *Hpb* infection (Figure S5A), but functional neutralization using an anti-IL-18 antibody had no effect on CD8$^+$ T cell IFNγ production (Figure S5F; confirmation of neutralization efficiency is shown in Figures S5G and S5H). IL-15 neutralization, while eliminating *Hpb*-induced NK cell recruitment to the SILP, also had no impact on the frequency of IFNγ$^+$ CD8$^+$ T cells or Sca-1 expression by IECs (Figures S5I–S5L). One compartment that has been previously implicated in intestinal CD8$^+$ T cell activation is the gut microbiota.[18] To directly test whether the gut microbiota was required for IFNγ production and ISG induction, we implemented our recently developed model of germ-free (GF) *Hpb* infection.[19] To this end, GF mice were infected with 200 GF *Hpb* larvae, and at 4 dpi, IFNγ and ISG expression were assessed. Littermate GF mice reconstituted with a specific pathogen-free (SPF) microbiota (i.e., conventionalized mice) were used as a positive control (Figure 3A). Importantly, we have previously shown that the adult worm burden and fecundity of GF *Hpb* are comparable to conventionally reared SPF larvae in both SPF and GF hosts.[19] Using this approach, we found that ISG induction and IFNγ by CD8$^+$ T cells were entirely dependent on the presence of the gut microbiota (Figures 3B–3D), whereas IFNγ production by CD4$^+$ T cells under these conditions did not change (Figure S5M). Helminth-infected GF mice phenocopied many features of infected *Ifngr*$^{-/-}$ mice, including the number, size, and hemorrhaging of detectable granulomas (Figures 3E, 3F, and S5N), as well as an overall shortening of the small intestine following a high-dose infection, compared with conventionalized controls (Figure 3G).

We next examined the role of MyD88, an intracellular adaptor protein critical for downstream signaling of most Toll-like

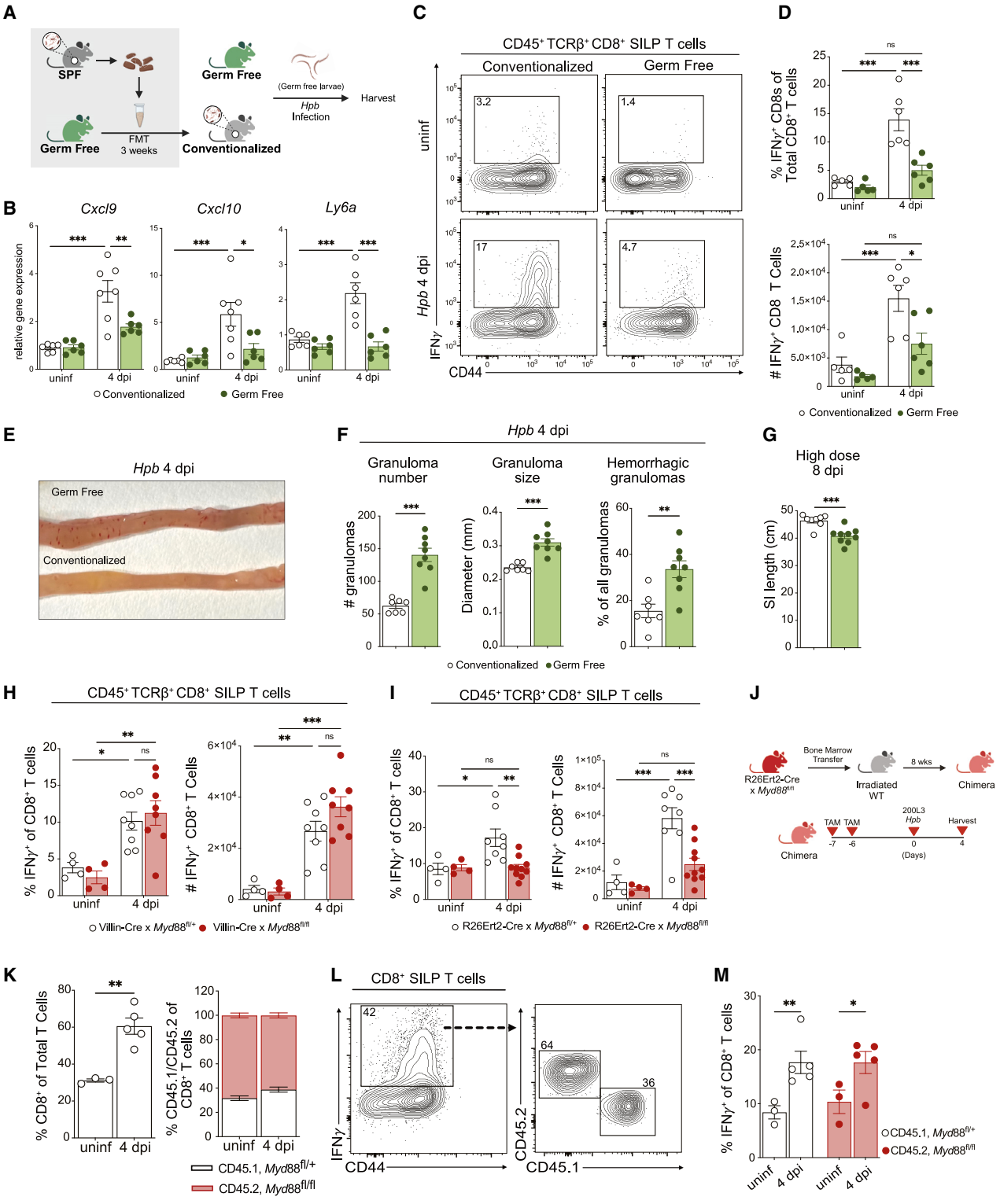

Figure 3. CD8+ T cell activation requires the gut microbiota and cell-extrinsic MyD88 signaling

(A) Schema for (B)–(G). Germ-free (GF) mice were gavaged with saline or fecal slurries from specific pathogen-free (SPF) mice 3 weeks prior to infection with 200 GF *Hpb* larvae.

(B) SILP ISG expression.

(legend continued on next page)

receptor (TLR) and IL-1R family members.[20] As a crucial cell interface between the microbiota and the immune system, we first deleted MyD88 signaling in the IEC compartment using Villin-cre x *Myd88*$^{fl/fl}$ animals. We found epithelial-derived MyD88 expression was dispensable for *Hpb*-induced IFNγ signaling (Figures 3H and S5O). By contrast, a systemic deletion approach using a tamoxifen-inducible Rosa26Ert2-cre x *Myd88*$^{fl/fl}$ mouse line collectively demonstrated that MyD88 signaling was absolutely required for IFNγ signaling in an epithelial cell-independent manner (Figures 3I and S5P). To test whether MyD88 signaling was intrinsic to the CD8$^+$ T cell compartment, we generated irradiation chimeras in which bone marrow cells from tamoxifen-inducible Rosa26Ert2-cre x *Myd88*$^{fl/fl}$ mice were transplanted into irradiated CD45.1 WT hosts (Figure 3J). Examination of these chimeras revealed an incomplete depletion of host CD45.1 CD8$^+$ Trm cells residing in the SILP, resulting in a mixed CD45.1 WT:CD45.2 *Myd88*$^{fl/fl}$ hematopoietic compartment (Figure 3K). Examining these mice as mixed chimeras, we determined that the activation of CD8$^+$ T cells occurred in a cell-extrinsic manner as IFNγ was produced by both CD45.1$^+$ (WT-derived) and CD45.2$^+$ (*Myd88*$^{fl/fl}$-derived) cells (Figures 3L and 3M). Therefore, *Hpb*-induced tissue invasion is not sufficient to induce IFNγ production but rather depends on the presence of the gut microbiota and CD8$^+$ T cell-extrinsic MyD88 signaling.

IFNγ signals recruit tissue-protective neutrophils to the site of *Hpb* infection

We next sought to understand how IFNγ signaling acts to limit tissue dysfunction and promote disease tolerance to *Hpb* infection. Immunofluorescence imaging of *Hpb*-infected tissue showed accumulation of CD8$^+$ T cells in proximity to the granulomas as compared with their dispersed localization in non-granuloma areas of *Hpb*-infected mice (Figure 4A). Consistent with this observation, immunohistochemical analyses of 2 dpi tissue indicated pervasive activation of STAT1 (pSTAT), a transcription factor critical for IFNγ target gene expression, surrounding the granulomas in IFNγR competent but not receptor-deficient mice (Figure 4B). Notably, pSTAT1 was detected in diverse cellular compartments, including immune, stromal, and epithelial cells. Since all cells express the IFNγR, we reanalyzed our previously published bulk RNA sequencing (RNA-seq) dataset from the intestine of day 2 *Hpb*-infected mice[6] to survey which cell types or pathways may contribute to the tissue-protective role of IFNγ production. Granulocyte migration and neutrophil migration, in particular, were highly upregulated as determined by Gene Ontology and gene set enrichment analysis (GSEA) (Figures 4C, 4D, and S6A). Highlighting genes related to neutrophils and their associated chemokines, a volcano plot of all the differentially expressed genes at 2 dpi showed that *Cxcl5* was among the most highly upregulated (Figure 4E). We validated this result by performing gene expression analysis of ISGs and *Cxcl5* in tissue biopsies from granuloma and non-granuloma regions of the *Hpb*-infected small intestine of *Ifngr*$^{+/+}$ and *Ifngr*$^{-/-}$ mice (Figures 4F and S6B). *In situ* hybridization revealed that *Cxcl5* transcripts were enriched around the granuloma at 4 dpi of *Ifngr*$^{+/+}$ mice but significantly decreased in *Ifngr*$^{-/-}$ mice (Figure 4G). Consistently, we observed a striking accumulation of Ly6G$^+$ neutrophils at the *Hpb* infection site that was abrogated in *Ifngr*$^{-/-}$ mice (Figure 4H), a phenotype also observed during GF *Hpb* infection (Figure S6C).

Neutrophils are early responders to infection with potent inflammatory and microbicidal activity.[21] However, substantial heterogeneity in neutrophil populations has been revealed,[22] including a growing appreciation for their tissue-protective functions.[23,24] To examine whether neutrophils impact tissue remodeling upon infiltration of the *Hpb* granuloma, we administered an anti-Ly6G neutrophil-depleting antibody from days −1 to 3 of infection. Remarkably, neutrophil depletion recapitulated many features of infected germline *Ifngr*$^{-/-}$ mice, including an increase in the size, number, and frequency of hemorrhagic granulomas (Figure 4I). Likewise, administration of an anti-Cxcl5 antibody to WT mice during *Hpb* infection attenuated neutrophil recruitment to the granuloma to a similar degree as that observed in *Ifngr*$^{-/-}$ mice (Figure 4J) and phenocopied the granulomatous phenotype (Figure S6D). By contrast, *Ccr2*$^{-/-}$ mice that lack Ly6C$^+$ circulating inflammatory monocytes[25] did not exhibit the same phenotype as neutrophil-depleted mice (Figures S6E–S6G). However, neutrophil-depleted mice challenged with a high dose of *Hpb* larvae did not succumb to infection (Figure S6H). These results indicate that IFNγ must act on distinct cellular compartments to ensure host survival during high-dose helminth infection.

IFNγ signaling recruits neutrophils to helminth granulomas in a cell-extrinsic manner

A recent study demonstrated that successful cancer immunotherapy was linked with a robust IFNγ gene signature in neutrophils that controlled tumor growth.[24] In this setting, anti-tumor

(C and D) (C) Representative contour plots pre-gated on viable CD45$^+$ TCRβ$^+$ CD8$^+$ SILP cells, quantified in (D).
(E and F) (E) Representative image of *Hpb* 4 dpi conventionalized or GF intestines with granuloma number, size, and frequency of hemorrhagic granulomas quantified in (F), scored blinded to the investigator.
(G–I) (G) Small intestinal length at day 8 following high-dose *Hpb* infection. Deletion of MyD88 signaling in the (H) intestinal epithelium (*Villin*-cre × *Myd88*$^{fl/fl}$) or (I) whole body (R26Ert2-cre × *Myd88*$^{fl/fl}$) compared with respective controls. SILP CD8$^+$ T cell production of IFNγ was quantified following *in vitro* PMA/ionomycin stimulation.
(J) Schema for hematopoietic deletion of Myd88 using bone marrow chimeras.
(K) Frequency of donor and host CD8$^+$ T cells (left) and percentage of host CD45.1 (*Myd88*$^{fl/+}$) and donor CD45.2 (*Myd88*$^{fl/fl}$) cells from the total populations (right).
(L) Representative contour plot of IFNγ$^+$ CD8$^+$ T cells, pre-gated on viable CD45$^+$ TCRβ$^+$ CD8$^+$ SILPs, and further gated into CD45.1$^+$ (host) and CD45.2$^+$ (donor) cells.
(M) Quantification of CD45.1 (host) or CD45.2 (donor) IFNγ$^+$ CD8$^+$ T cells from (L). Pooled results from 2–3 independent experiments, n = 6–10 per group. Between-group comparisons were analyzed using nonparametric Student's t tests and time course analyses using one- or two-way ANOVA with Tukey's post hoc analysis. *$p < 0.05$, **$p < 0.01$, and ***$p < 0.001$; ns, not significant.
See also Figure S5.

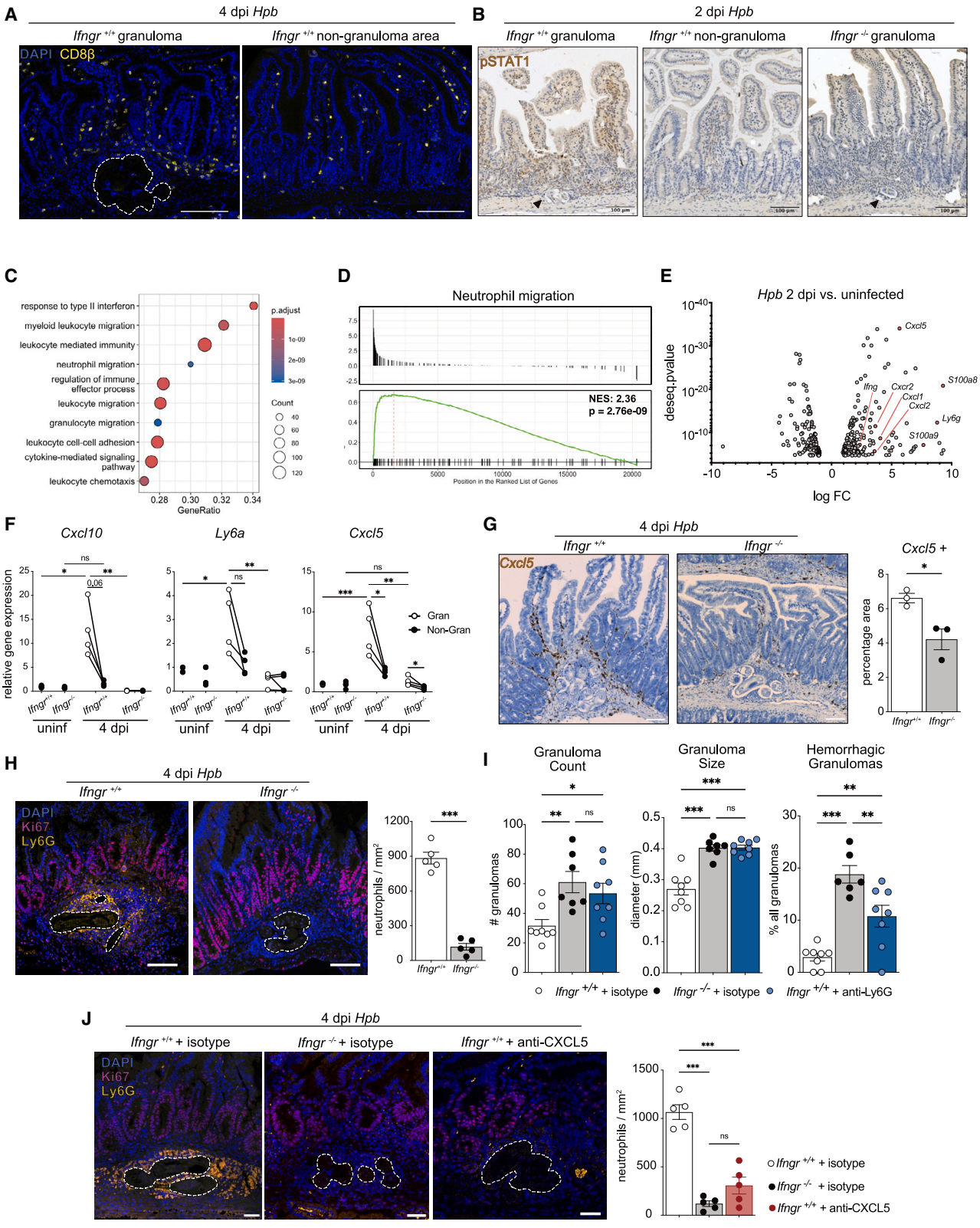

(legend on next page)

neutrophils were identified as expressing low amounts of Siglec-F compared with their pro-tumor counterparts.[24] To investigate whether this neutrophil phenotype also applies to infection, we first examined Sca-1 expression on infiltrating innate immune cells. Whereas Ly6C$^+$ monocytes highly expressed Sca-1 in an IFNγR-dependent manner, neutrophils failed to express this IFNγ target gene (Figure 5A). Interestingly, when we assessed Siglec-F expression, neutrophils from *Ifngr*$^{+/+}$ mice expressed significantly less Siglec-F compared with the neutrophils we recovered from *Ifngr*$^{-/-}$ mice (Figure 5B), suggesting that they may be amenable to IFNγ-mediated immunomodulation. To definitively determine whether direct IFNγ signaling in neutrophils was required for their recruitment to *Hpb* granulomas, we constructed reciprocal irradiation chimeras where *Ifngr*$^{+/+}$ or *Ifngr*$^{-/-}$ bone marrow cells were transplanted into either irradiated *Ifngr*$^{+/+}$ or *Ifngr*$^{-/-}$ mice (WT-knockout (KO) and KO-WT; Figure 5C). Genotype-matched (WT-WT and KO-KO) chimeras were generated as controls. As expected, there was a strong ISG signature at day 4 in the WT-WT control chimeras that was absent in the KO-KO group. However, the KO-WT group, with an IFNγR-competent radioresistant compartment, retained ISG expression while the WT-KO group did not (Figure 5D). Consistently, the loss of an IFNγ signature in the WT-KO chimeras, but not the KO-WT group, was associated with a defect in neutrophil recruitment (Figures 5E and 5F). These results indicated that IFNγ signaling on a radioresistant cell population is required for neutrophil recruitment.

Direct sensing of IFNγ by the intestinal stroma mediates neutrophil recruitment and tissue preservation during infection

Recently, the intestinal epithelium has been shown to integrate IFNγ signals to mediate host defense against bacterial infection and tumor immunity.[26] To test whether the intestinal epithelium was the radioresistant population sensitive to IFNγ signals during *Hpb* infection, we generated Villin-cre x *Ifngr*$^{fl/fl}$ mice that failed to induce Sca-1 through IFNγ signaling in the intestinal epithelium (Figure S6I). At day 4, there were no defects in the early granulomatous damage phenotype (Figure S6J) nor was there elevated mortality in high-dose infected mice compared with littermate controls (Figure S6K). Neutrophil recruitment was also intact in Villin-cre x *Ifngr*$^{fl/fl}$ mice (Figure S6L), indicating that the epithelium is not involved in IFNγ-mediated tissue protection or disease tolerance during *Hpb* infection.

An additional radioresistant population in mice is the stromal cells. The stroma is a heterogeneous cell compartment typically associated with production of the extracellular matrix.[27] Recently, the immunomodulatory properties of the stroma have become more appreciated in response to injury,[28] infection,[29,30] and in mesenchymal stem cell therapy.[31] As an initial examination of the intestinal stroma during *Hpb* infection, alpha smooth muscle actin (αSMA)-producing cells were visualized at day 4 by immunofluorescence microscopy. As expected, the muscularis propria was densely populated by αSMA$^+$ cells in *Ifngr*$^{+/+}$ and *Ifngr*$^{-/-}$ mice. However, in the absence of IFNγ signals, there was substantial remodeling of the stromal cells with significant accumulation of αSMA-producing cells surrounding the granuloma and extending throughout the intestinal villi that was not observed in *Hpb*-infected *Ifngr*$^{+/+}$ mice (Figure 6A), a result that remained even with the additional inhibition of IL-4 and IL-13 neutralization (Figure S6M). We obtained similar results in GF *Hpb*-infected mice compared with their conventionalized controls (Figure S6N). To determine whether direct IFNγ sensing by the stromal cell compartment regulated αSMA-producing cells, we crossed mice expressing a tamoxifen-inducible cre recombinase under control of the smooth muscle myosin Myh11 (Myh11Ert2-cre) with our *Ifngr*$^{fl/fl}$ mouse line to generate Myh11Ert2-cre x *Ifngr*$^{fl/fl}$ animals. Importantly, Myh11 and αSMA expression overlap within the small intestinal mesenchyme and include various smooth muscle and fibroblast subsets.[27] Similar to the germline *Ifngr*$^{-/-}$ mice, we observed an increase in αSMA staining in Myh11Ert2-cre x *Ifngr*$^{fl/fl}$ but not Myh11Ert2-cre x *Ifngr*$^{fl/+}$ littermate controls at day 4 (Figure 6B). Furthermore, eliminating IFNγ signaling in this stromal cell compartment reduced *Cxcl5* expression (Figure 6C) and neutrophil recruitment (Figure 6D) in the vicinity of the granuloma. To directly assess whether stromal cells express *Cxcl5* mRNA, we crossed Myh11Ert2-Cre mice with Rosa26lsl-Tdtomato mice and combined detection of tomato$^+$ cells with *in situ* single gene transcript identification. Indeed, a population of tomato$^+$

Figure 4. IFNγ-mediated neutrophil recruitment limits tissue damage during early *Hpb* infection

(A) Representative immunofluorescence image of CD8$^+$ T cell localization in *Ifngr*$^{+/+}$ mice. Granuloma is highlighted in a white hashed line. DAPI, blue; CD8β, yellow; scale bar, 100 μm.

(B) Representative immunohistochemistry image of pSTAT1 staining in *Ifngr*$^{+/+}$ granuloma (left), non-granuloma (middle), and *Ifngr*$^{-/-}$ mice (right). Black arrows indicate granulomas; scale bar, 100 μm.

(C) Top differentially expressed Gene Ontology terms at 2 dpi compared with uninfected controls following bulk RNA-seq analysis of whole small intestinal tissue.

(D and E) (E) Gene set enrichment analysis (GSEA) and normalized enrichment score (NES) for neutrophil migration and (E) volcano plot highlighting upregulated neutrophil-related genes. FC, fold change.

(F) Gene expression of biopsies taken from granuloma (open circles) and non-granuloma (closed circles) regions of *Ifngr*$^{+/+}$ and *Ifngr*$^{-/-}$ mice.

(G) *Cxcl5 in situ* hybridization in granuloma areas; scale bar, 50 μm (left), quantified as a percentage of positive pixels per granuloma area (right). Each dot averages 3–5 granulomas from three mice.

(H) Immunofluorescent imaging (Ly6G, yellow; Ki67, pink; DAPI, blue) of granulomas (left) quantified as the number of neutrophils per granuloma area (right). Each dot averages 3–5 granulomas. Scale bar, 50 μm.

(I) Number, size, and frequency of hemorrhagic granulomas in isotype- or anti-Ly6G-treated mice at 4 dpi, scored blinded.

(J) Immunofluorescent imaging and quantification as in (H) but with *Ifngr*$^{+/+}$ mice treated with anti-Cxcl5 antibody or isotype control. Pooled results from 2–3 independent experiments, $n = 6$–10 mice per group. Scale bar, 50 μm. Between-group comparisons were analyzed with nonparametric Student's t tests or paired analysis (F). $^*p < 0.05$, $^{**}p < 0.01$, $^{***}p < 0.001$; ns, not significant.

See also Figure S6.

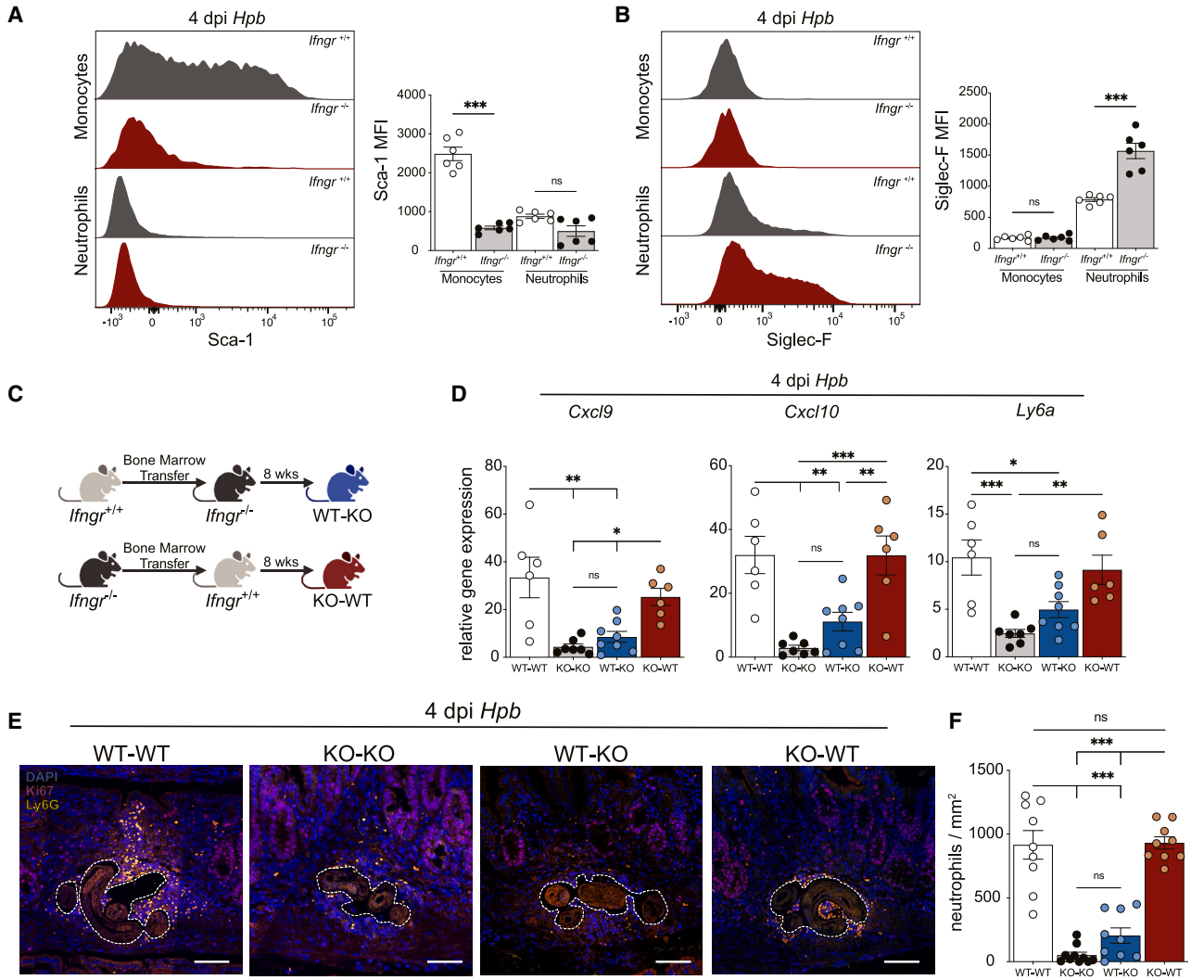

Figure 5. IFNγ recruits tissue-protective neutrophils to *Hpb* granulomas in a cell-extrinsic manner

(A and B) Representative histograms of (A) Sca-1 and (B) Siglec-F expression (MFI) by intestinal monocytes (CD45$^+$ CD11b$^+$ MHCII^{lo} Ly6C^{hi}) and neutrophils (CD45$^+$ CD11b$^+$ Ly6G$^+$) (left) with quantification (right).

(C) Schema of bone marrow chimera approach with WT-WT and KO-KO controls not shown.

(D–F) (D) ISG expression, (E) representative immunofluorescence images (Ly6G$^+$, yellow; Ki67, pink; DAPI, blue; scale bar, 50 μm), and (F) quantification of intestinal neutrophils in respective chimera groups. Each dot averages 3–5 granulomas per mouse. Two independent pooled experiments, n = 8–10 mice per group. Between-group comparisons were analyzed with Student's t tests. *$p < 0.05$, **$p < 0.01$, ***$p < 0.001$; ns, not significant.

cells co-expressed *Cxcl5* at the site of *Hpb* infection (Figure 6E). Furthermore, stimulation of primary intestinal αSMA$^+$Vimentin$^+$ myofibroblasts with recombinant IFNγ rapidly induced ISGs and *Cxcl5*,but not other quintessential neutrophil chemokines such as *Cxcl1* and *Cxcl2* (Figures 6F and 6G) or *Ccl2* and *Ccl3* (Figure S6O). Combining these results with our gene expression analyses of tissue biopsies (Figures 4F and S6B) indicates that the intestinal stroma is highly responsive to IFNγ signals and expresses a gene signature that supports neutrophil recruitment via Cxcl5 production.

Using outcomes of parasite-induced damage that we measured in *Hpb*-infected germline *Ifngr*$^{-/-}$ mice, GF mice, and neutrophil-depleted mice, we also found that the number, size, and frequency of hemorrhagic granulomas were all increased in Myh11Ert2-cre x *Ifngr*$^{fl/fl}$ compared with littermate controls (Figure 6H). Similar results were observed in *Hpb*-infected mice lacking the IFNγR in Collagen1A2-expressing stromal cells (Col1A2Ert2-cre x *Ifngr*$^{fl/fl}$ mice; Figure S6P). Upon challenge with a high dose of *Hpb* larvae, Myh11Ert2-cre x *Ifngr*$^{fl/fl}$ also experienced a higher rate of mortality compared with controls (Figure 6I), without any difference in worm burden (Figures 6J and S6Q). Finally, assessment of intestinal transit and small intestinal length prior to the expected onset of mortality phenocopied the defects observed in germline *Ifngr*$^{-/-}$ mice (Figures 6K and 6L). Collectively, our data indicate that direct IFNγ signaling into the intestinal stroma promotes

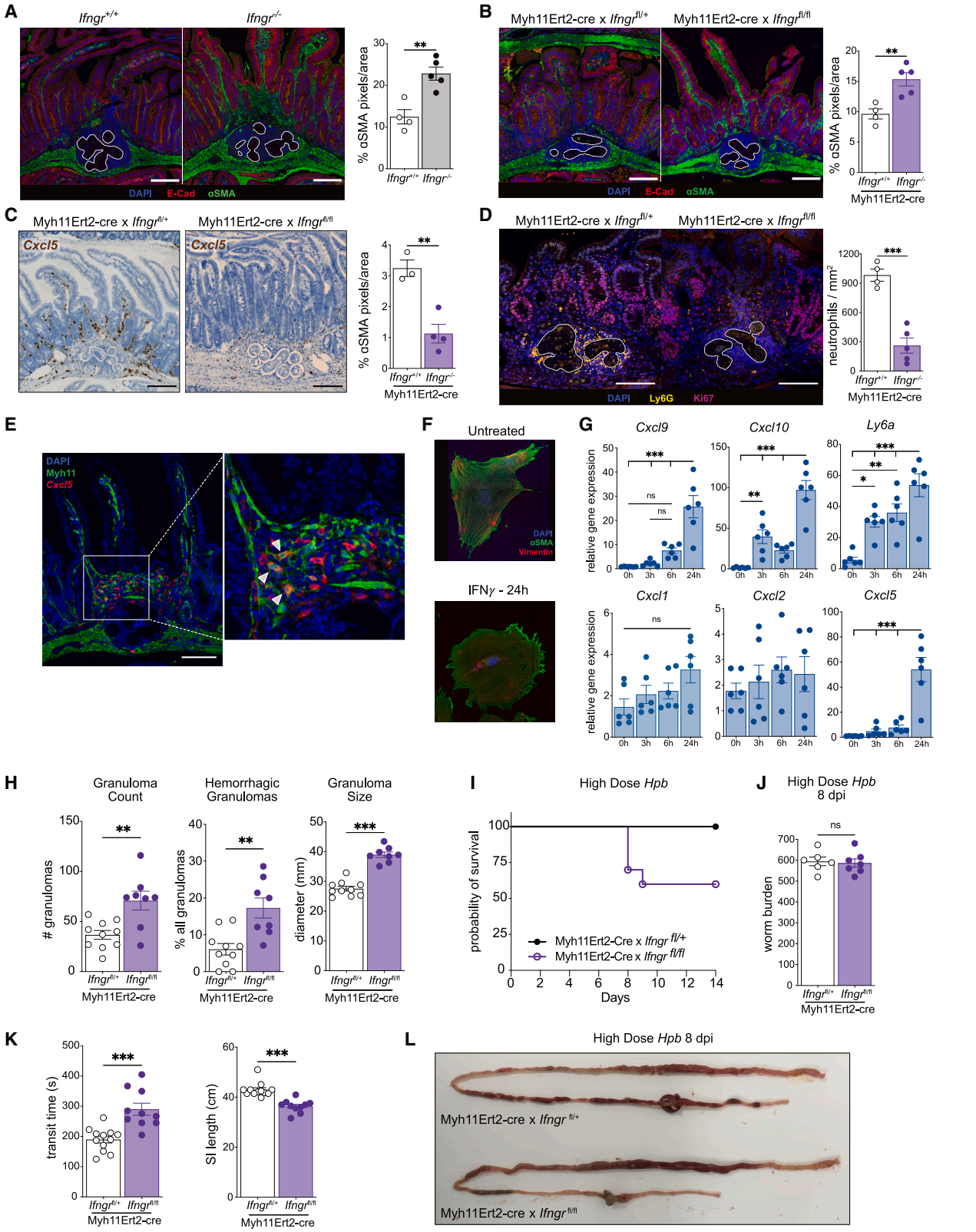

(legend on next page)

disease tolerance to infection by recruiting tissue-protective neutrophils and restraining elaboration of the smooth muscle actin-expressing cell network to prevent pathological gut dysmotility.

DISCUSSION

Type 1 immunity involves a multicellular sensing and signaling network indispensable for protection against intracellular pathogens.[32] A central effector molecule in this defense pathway is IFNγ, first identified by its potent ability to "interfere" with viral replication in leukocytes.[33] This function as well as many others, including the amplification of anti-bacterial and anti-protozoan immunity as well as a more recent measure of successful cancer immunotherapy, has continued to draw attention to this cytokine for over half a century.[34] However, pathogen elimination, also known as host resistance, is only one defense strategy against infection. A complementary or alternative defense strategy is disease tolerance. First described by plant biologists over a century ago[35] and now being investigated in mammals, including humans,[36,37] disease tolerance is defined as the host's ability to control tissue damage without reducing pathogen load[1]. Although studies have identified immune cell-intrinsic checkpoints[38] and metabolic resilience[39–41] as ways to support this defense strategy, a role for immune-stromal cell networks has not been described. Our study reveals that, in addition to its robust anti-microbial activity, IFNγ is also fundamental to disease tolerance by preserving tissue function during infection. These data align with the concept that disruptions, not only to host immunity but also to tissue physiology (e.g., intestinal transit time and regulation of blood glucose levels), can impact disease tolerance to infection[1].

Despite the global prevalence of intestinal helminths, knowledge of the tissue response during the earliest events of infection remains nebulous compared with other pathogens. Here, we use *Hpb* infection that follows a well-defined kinetic of infection in the small intestine to investigate how a multicellular parasite is tolerated by the host. Our results build on previous studies demonstrating that the early tissue-invasive phase of *Hpb* infection is defined by a type 1 immune response[6–8] and that the absence of this pathway impacts granuloma resolution and host resistance during the chronic stages of infection.[12,42,43] We now demonstrate that $CD8^+$ αβ T cells residing in the SLIP are the primary source of IFNγ production during early *Hpb* infection. Our results also indicate that, in this context, cognate antigen encounter was not required. However, the presence of the gut microbiota was critical, indicating that these cells were responding in an innate-like manner for host defense. Although antigen-independent differentiation and maintenance of $CD8^+$ Trm cells has been previously shown,[16,44] the ability of the microbiota to induce tissue-protective activity by this subset has not been described. We also found that hematopoietic cell sensing of the microbiota was required in a T cell-extrinsic, MyD88-dependent pathway. Additional gnotobiotic and cell-specific gene-targeting approaches are needed to reveal the signaling network leading to Trm cell activation in this context.

Intestinal dysfunction affects up to a third of the Western population, with a significant proportion involving severe dysmotility.[45] Many of these conditions are associated with recent intestinal infections, inflammatory events, or post-surgical complications, while others remain "idiopathic."[46] Upon high-dose *Hpb* infection, we observed that mice with a germline or stromal cell-specific deletion of IFNγR demonstrated quantitative small intestinal dysmotility. Type 1 cytokines have been linked to hypocontractility of gut smooth muscle[47] with IFNγ directly inhibiting αSMA production by arterial smooth muscle cells *in vitro*.[48] Functionally, IFNγ decreased longitudinal muscle contractility ex vivo[47] and reduced contractibility and proliferation of human-derived intestinal smooth muscle cells.[49] Likewise, *Trichinella spiralis* infection of mice exhibiting elevated IFNγ production resulted in muscle hypocontractility.[50] The regulatory impact of IFNγ on smooth muscle contractility serves as an additional example of the mutual antagonistic nature of type 1 and type 2 cytokines,[13] as it is well-known that the latter, including IL-4 and IL-13, enhance contractility to promote the weep and

Figure 6. Stromal cell-intrinsic IFNγ signaling orchestrates disease tolerance to *Hpb* infection

(A) Representative immunofluorescence images of granuloma regions visualized with alpha smooth muscle actin (αSMA, green), E-cadherin (red), and DAPI (blue) staining (left) with quantification of αSMA-positive pixels to total granuloma-associated tissue area (right). Each dot averages 2–3 granulomas per mouse; scale bar, 50 μm.

(B) Same as (A) in Myh11Ert2-cre × *Ifngr*$^{fl/fl}$ mice and controls (Myh11Ert2-cre × *Ifngr*$^{fl/+}$).

(C) *Cxcl5 in situ* hybridization of Myh11Ert2-cre × *Ifngr*$^{fl/fl}$ mice (left) with quantification of transcript-positive signal per unit area (right). Scale bar, 50 μm. One experiment, n = 4–5 mice per group, and each dot averages 2–5 granulomas per mouse.

(D) Immunofluorescent imaging (Ly6G, yellow; Ki67, pink; DAPI, blue; scale bar, 50 μm) in Myh11Ert2-cre × *Ifngr*$^{fl/fl}$ mice or littermate control animals (left) with quantification (right). Each dot averages 3–5 granulomas per mouse.

(E) Representative co-labeling of *Cxcl5* mRNA (*in situ* hybridization; red) and $Myh11^+$ cells via tdTomato detection (green). Colocalization highlighted with white arrows.

(F) Representative images of primary fibroblasts derived from uninfected small intestines of C57BL/6 mice unstimulated (top) or following 24 h of rIFNγ treatment (bottom) labeled with DAPI (blue), αSMA (green), and vimentin (red).

(G) Gene expression of IFNγ-stimulated fibroblasts.

(H) Quantification of visible granuloma number, hemorrhagic frequency, and size at 4 dpi between Myh11Ert2-cre × *Ifngr*$^{fl/fl}$ mice and littermate controls, scored blinded.

(I and J) (I) Kaplan-Meier survival curves of high-dose infected Myh11Ert2-cre × *Ifngr*$^{fl/fl}$ mice and littermate controls with worm burden at 8 dpi (J).

(K and L) (K) Transit time (left), intestinal length (right), and (L) representative intestinal morphology images. Pooled results from 2–3 independent experiments, n = 6–10 mice per group, unless otherwise stated. Between-group comparisons were analyzed with nonparametric Student's t tests. $^*p < 0.05$, $^{**}p < 0.01$, $^{***}p < 0.001$; ns, not significant.

See also Figure S6.

sweep response during helminth infection[51] and protect from infection-induced dysmotility.[52] Indeed, the absence of IFNγ has been shown to increase *Hpb* expulsion at the later time points of infection (28 dpi),[12] a finding that we reproduced. Examining the early time points in which a type 1 immune response is dominant, however, we did not observe a significant difference in worm burden in the presence or absence of IFNγ signals. Consistently, additional neutralization of IL-4 and IL-13 within the first week of *Hpb* infection had no discernible impact on granuloma size, hemorrhaging, or intestinal motility, suggesting that induction of type 1 cytokine signaling is not simply used as an immune evasion strategy by the parasite but may be more relevant for preserving tissue function. Consistent with these results, loss of IFNγR signaling in Sox10-expressing enteric glial cells during *Hpb* infection was recently shown to also compromise gut motility.[8] This study reported that enteric glial cell-intrinsic IFNγ signals promoted resolution of granulomas and, in combination with previous studies,[12,43] indicate that IFNγ also contributes to tissue repair during chronic infection. Given the transient induction of IFNγ and its associated target genes during the early stage of infection, these data suggest that brief activation of type 1 immunity may have long-term impacts on wound healing, applicable to other settings of dysregulated repair and fibrosis such as ulcerative colitis.

Gut motility disorders are commonly associated with enteric nervous system (ENS) dysfunction, and, in contrast to our results, $CD8^+$ T cell production of IFNγ can aggravate dysmotility.[53,54] In these instances, the effects were due to direct regulation of enteric neuron density and signaling. However, distinct mechanisms underlie gut dysmotility. Infection of mice with the roundworm *Nippostrongylus brasiliensis* led to hypercontractility of the small intestine that was independent of the ENS, confirming the importance of the stroma as an additional mediator of gut motility.[55] Stratifying disease based on the form or cell types driving gut dysmotility may allow for more personalized approaches to treat this morbidity.

We also observed a direct link between stroma-intrinsic IFNγR signaling and neutrophil recruitment to the site of infection. Stromal-neutrophil communication is an understudied field, though recent studies highlight the importance of the extracellular matrix in regulating leukocyte chemotaxis during mucosal tissue damage.[56] Our data indicate that IFNγ acts directly on αSMA^+ cells to mediate neutrophil chemotaxis through *Cxcl5* expression. This response parallels a recent finding where skin stromal cells upregulated a set of immunomodulatory and repair transcripts following acute tissue damage.[29] Among these transcripts was *Cxcl5*, and blockade of this chemokine led to protracted inflammation.[28] Similarly, $Cxcl12^+$ fibroblasts recruit neutrophils to cutaneous *Staphylococcus aureus* infection through the detection of IL-17.[29] Additionally, successful cancer immunotherapy was recently associated with local neutrophil recruitment to the tumor site,[24] supporting the notion that IFNγ sensing by stromal cells could be a prime mediator of neutrophil recruitment. Although we demonstrated that neutrophils limit excessive damage to the vasculature to minimize tissue hemorrhage and initiate wound healing, their depletion did not result in mortality following high-dose *Hpb* challenge as observed by eliminating IFNγ signaling in the germline or Myh11-expressing cells. Although this result may stem from the technical inability to completely deplete rapidly renewing neutrophils over a prolonged period of time (e.g., more than 3–4 days), we hypothesize that neutrophil recruitment is important for tissue damage control and proper wound healing[23] but not critical for host survival under these conditions. By contrast, the regulation of intestinal motility by IFNγ-dependent stromal cell activation is necessary to preserve tissue function and survival. We cannot rule out other effects the stroma may have on tissue integrity that support disease tolerance during *Hpb* infection.

Finally, our data dovetail with studies showing a tissue-protective role for type 1 immunity in other contexts. For example, epithelial cell-intrinsic IFNγ signaling during intestinal bacterial infection and inflammation inhibited inflammasome activation responsible for driving $CD4^+$ T cell-mediated colonic barrier damage.[26] Importantly, the tissue-protective effects of IFNγ had no impact on pathogen burden, indicating another setting in which IFNγ supports disease tolerance.[26] In addition, neutralization of IFNγ during pulmonary fungal infection of mice prevented lung damage while enhancing pathogen clearance, suggesting that IFNγ can simultaneously impact disease tolerance and host resistance pathways.[57] Moreover, IFNγ can also protect from immunopathology in non-infectious disease settings. IFNγ signaling has been shown to limit alloreactive T cell responses during transplantation by inducing indolemine 2,3-dioxygenase in antigen-presenting cells, which blunts T cell expansion.[58] In addition, the presence of IFNγ is associated with neutrophil recruitment and regeneration following peripheral nerve injury.[59] Elegant *in vitro* studies have also revealed that human $CD8^+$ T cell production of IFNγ can support epithelial tissue remodeling and wound healing by sensitizing cells to the tissue repair factor, amphiregulin.[60] Combining these studies with our data provides the impetus for re-evaluating how a cytokine, regarded to strictly drive inflammation and pathogen killing, can support adaptive tissue responses during injury and insult.

Limitations of the study

Although our data identify IFNγ signaling as critical for disease tolerance to an enteric pathogen in a mouse model, the importance of this pathway to helminth infection in a natural setting requires validation. In addition, identifying how granuloma-associated neutrophils promote vascular integrity during *Hpb* infection remains to be defined. Evaluating the relevance of this immune-stromal network in other intestinal disorders of motility, such as the post-infectious state (“irritable bowel syndrome”)[61] or the aged state,[62] may be informative. Finally, the specific origin of the myosin (Myh11)-expressing cells within the broader stromal compartment remains to be determined.

RESOURCE AVAILABILITY

Lead contact

Further information and requests for resources and reagents should be directed to and will be fulfilled by the lead contact, Irah King (irah.king@mcgill.ca).

Materials availability

This study did not generate new, unique reagents.

Data and code availability

- Previously published RNA-seq data[6] have been deposited at NCBI Gene Expression Omnibus as GEO: GSE292516 and are publicly available as of the date of publication.
- Microscopy data reported in this paper will be shared by the lead contact upon request.
- All original code is available in this paper's methods section.
- Any additional information required to reanalyze the data reported in this paper is available from the lead contact upon request.

ACKNOWLEDGMENTS

We thank the staff of the animal, histopathological, and immunophenotyping platforms at the Research Institute of the McGill University Health Centre. Special thanks to Cynthia Faubert and Catherine Hudon for their assistance with the germ-free animal studies and the McGill Interdisciplinary Initiative in Infection and Immunity for financial support to establish the Gnotobiotic Animal Research Platform at the RI-MUHC. We also appreciate the Meakins-Christie Laboratories administration and Séverine Audusseau for technical support. S. Westfall is the recipient of a Canadian Institutes of Health Research (CIHR) Postdoctoral Fellowship (MFE-181759). I.L.K. is a recipient of a Fonds de Recherche du Québec Scholar Award. M.E.G. is a recipient of a Fonds de Recherche du Québec Postdoctoral Award. S. Weis is currently funded by the Deutsche Forschungsgemeinschaft, DFG, project number WE 4971/6-1 and 9-1; the Excellence Cluster Balance of the Microverse (EXC 2051 and 390713860); and the Federal Ministry of Education and Research (BMBF) project number 01EN2001. This work was supported by CIHR (PJT-178182) to I.L.K.

AUTHOR CONTRIBUTIONS

Conceptualization, S. Westfall, M.E.G., and I.L.K.; methodology, S. Westfall, M.E.G., T.M.O., F.R., R.D.P., D.K.-A., G.F., D.H., M.J.R., G.M., J.F.E.K., O.J.H., M.D., A.G., and I.L.K.; software, A.B.; formal analysis, S. Westfall, M.E.G., T.M.O., A.B., G.M., D.K.-A., and I.L.K.; investigation, S. Westfall, M.E.G., T.M.O., F.R., R.D.P., D.K.-A., G.M., G.F., and I.L.K.; resources, F.R., G.F., D.H., H.J.M., V.A., M.J.R., O.J.H., M.D., S. Weis, A.G., and I.L.K.; writing – original draft, S. Westfall and I.L.K.; writing – review & editing, all authors; visualization, S. Westfall, A.B., and I.L.K.; funding acquisition, I.L.K.

DECLARATION OF INTERESTS

The authors have no interests to declare.

STAR★METHODS

Detailed methods are provided in the online version of this paper and include the following:

Received: April 1, 2024
Revised: December 3, 2024
Accepted: March 26, 2025
Published: April 22, 2025

REFERENCES

1. Medzhitov, R., Schneider, D.S., and Soares, M.P. (2012). Disease tolerance as a defense strategy. Science *335*, 936–941. https://doi.org/10.1126/science.1214935.
2. King, I.L., and Li, Y. (2018). Host-Parasite Interactions Promote Disease Tolerance to Intestinal Helminth Infection. Front. Immunol. *9*, 2128. https://doi.org/10.3389/fimmu.2018.02128.
3. Hotez, P.J., Brindley, P.J., Bethony, J.M., King, C.H., Pearce, E.J., and Jacobson, J. (2008). Helminth infections: the great neglected tropical diseases. J. Clin. Invest. *118*, 1311–1321. https://doi.org/10.1172/JCI34261.
4. Palm, N.W., Rosenstein, R.K., and Medzhitov, R. (2012). Allergic Host Defenses. Nature *484*, 465–472. https://doi.org/10.1038/nature11047.
5. Finlay, C.M., Parkinson, J.E., Zhang, L., Chan, B.H.K., Ajendra, J., Chenery, A., Morrison, A., Kaymak, I., Houlder, E.L., Murtuza Baker, S., et al. (2023). T helper 2 cells control monocyte to tissue-resident macrophage differentiation during nematode infection of the pleural cavity. Immunity *56*, 1064–1081.e10. https://doi.org/10.1016/j.immuni.2023.02.016.
6. Gentile, M.E., Li, Y., Robertson, A., Shah, K., Fontes, G., Kaufmann, E., Polese, B., Khan, N., Parisien, M., Munter, H.M., et al. (2020). NK cell recruitment limits tissue damage during an enteric helminth infection. Mucosal Immunol. *13*, 357–370. https://doi.org/10.1038/s41385-019-0231-8.
7. Nusse, Y.M., Savage, A.K., Marangoni, P., Rosendahl-Huber, A.K.M., Landman, T.A., de Sauvage, F.J., Locksley, R.M., and Klein, O.D. (2018). Parasitic helminths induce fetal-like reversion in the intestinal stem cell niche. Nature *559*, 109–113. https://doi.org/10.1038/s41586-018-0257-1.
8. Progatzky, F., Shapiro, M., Chng, S.H., Garcia-Cassani, B., Classon, C.H., Sevgi, S., Laddach, A., Bon-Frauches, A.C., Lasrado, R., Rahim, M., et al. (2021). Regulation of intestinal immunity and tissue repair by enteric glia. Nature *599*, 125–130. https://doi.org/10.1038/s41586-021-04006-z.
9. Ivashkiv, L.B. (2018). IFNγ: signalling, epigenetics and roles in immunity, metabolism, disease and cancer immunotherapy. Nat. Rev. Immunol. *18*, 545–558. https://doi.org/10.1038/s41577-018-0029-z.
10. Prakash, A., Monteith, K.M., and Vale, P.F. (2022). Mechanisms of damage prevention, signalling and repair impact disease tolerance. Proc. R. Soc. B. *289*, 20220837. https://doi.org/10.1098/rspb.2022.0837.
11. Maizels, R.M., Hewitson, J.P., Murray, J., Harcus, Y.M., Dayer, B., Filbey, K.J., Grainger, J.R., McSorley, H.J., Reynolds, L.A., and Smith, K.A. (2012). Immune modulation and modulators in Heligmosomoides polygyrus infection. Exp. Parasitol. *132*, 76–89. https://doi.org/10.1016/j.exppara.2011.08.011.
12. Reynolds, L.A., and Maizels, R.M. (2012). Cutting edge: in the absence of TGF-β signaling in T cells, fewer CD103+ regulatory T cells develop, but exuberant IFN-γ production renders mice more susceptible to helminth

infection. J. Immunol. *189*, 1113–1117. https://doi.org/10.4049/jimmunol.1200991.

13. Abbas, A.K., Murphy, K.M., and Sher, A. (1996). Functional diversity of helper T lymphocytes. Nature *383*, 787–793. https://doi.org/10.1038/383787a0.
14. Perona-Wright, G., Mohrs, K., and Mohrs, M. (2010). Sustained signaling by canonical helper T cell cytokines throughout the reactive lymph node. Nat. Immunol. *11*, 520–526. https://doi.org/10.1038/ni.1866.
15. Reinhardt, R.L., Liang, H.-E., and Locksley, R.M. (2009). Cytokine-secreting follicular T cells shape the antibody repertoire. Nat. Immunol. *10*, 385–393. https://doi.org/10.1038/ni.1715.
16. Casey, K.A., Fraser, K.A., Schenkel, J.M., Moran, A., Abt, M.C., Beura, L.K., Lucas, P.J., Artis, D., Wherry, E.J., Hogquist, K., et al. (2012). Antigen-Independent Differentiation and Maintenance of Effector-like Resident Memory T Cells in Tissues. J. Immunol. *188*, 4866–4875. https://doi.org/10.4049/jimmunol.1200402.
17. Matloubian, M., Lo, C.G., Cinamon, G., Lesneski, M.J., Xu, Y., Brinkmann, V., Allende, M.L., Proia, R.L., and Cyster, J.G. (2004). Lymphocyte egress from thymus and peripheral lymphoid organs is dependent on S1P receptor 1. Nature *427*, 355–360. https://doi.org/10.1038/nature02284.
18. Tanoue, T., Morita, S., Plichta, D.R., Skelly, A.N., Suda, W., Sugiura, Y., Narushima, S., Vlamakis, H., Motoo, I., Sugita, K., et al. (2019). A defined commensal consortium elicits CD8 T cells and anti-cancer immunity. Nature *565*, 600–605. https://doi.org/10.1038/s41586-019-0878-z.
19. Russell, G.A., Peng, G., Faubert, C., Verdu, E.F., Hapfelmeier, S., and King, I.L. (2021). A protocol for generating germ-free Heligmosomoides polygyrus bakeri larvae for gnotobiotic helminth infection studies. STAR Protoc. *2*, 100946. https://doi.org/10.1016/j.xpro.2021.100946.
20. Deguine, J., and Barton, G.M. (2014). MyD88: a central player in innate immune signaling. F1000Prime Rep. *6*, 97. https://doi.org/10.12703/P6-97.
21. Nathan, C. (2006). Neutrophils and immunity: challenges and opportunities. Nat. Rev. Immunol. *6*, 173–182. https://doi.org/10.1038/nri1785.
22. Aroca-Crevillén, A., Vicanolo, T., Ovadia, S., and Hidalgo, A. (2024). Neutrophils in Physiology and Pathology. Annu. Rev. Pathol. *19*, 227–259. https://doi.org/10.1146/annurev-pathmechdis-051222-015009.
23. Phillipson, M., and Kubes, P. (2019). The Healing Power of Neutrophils. Trends Immunol. *40*, 635–647. https://doi.org/10.1016/j.it.2019.05.001.
24. Gungabeesoon, J., Gort-Freitas, N.A., Kiss, M., Bolli, E., Messemaker, M., Siwicki, M., Hicham, M., Bill, R., Koch, P., Cianciaruso, C., et al. (2023). A neutrophil response linked to tumor control in immunotherapy. Cell *186*, 1448–1464.e20. https://doi.org/10.1016/j.cell.2023.02.032.
25. Serbina, N.V., and Pamer, E.G. (2006). Monocyte emigration from bone marrow during bacterial infection requires signals mediated by chemokine receptor CCR2. Nat. Immunol. *7*, 311–317. https://doi.org/10.1038/ni1309.
26. Malik, A., Sharma, D., Aguirre-Gamboa, R., McGrath, S., Zabala, S., Weber, C., and Jabri, B. (2023). Epithelial IFNγ signalling and compartmentalized antigen presentation orchestrate gut immunity. Nature *623*, 1044–1052. https://doi.org/10.1038/s41586-023-06721-1.
27. McCarthy, N., Tie, G., Madha, S., He, R., Kraiczy, J., Maglieri, A., and Shivdasani, R.A. (2023). Smooth muscle contributes to the development and function of a layered intestinal stem cell niche. Dev. Cell *58*, 550–564.e6. https://doi.org/10.1016/j.devcel.2023.02.012.
28. Yaghi, O.K., Hanna, B.S., Langston, P.K., Michelson, D.A., Jayewickreme, T., Marin-Rodero, M., Benoist, C., and Mathis, D. (2023). A discrete 'early-responder' stromal-cell subtype orchestrates immunocyte recruitment to injured tissue. Nat. Immunol. *24*, 2053–2067. https://doi.org/10.1038/s41590-023-01669-w.
29. Cavagnero, K.J., Li, F., Dokoshi, T., Nakatsuji, T., O'Neill, A.M., Aguilera, C., Liu, E., Shia, M., Osuoji, O., Hata, T., et al. (2024). CXCL12+ dermal fibroblasts promote neutrophil recruitment and host defense by recognition of IL-17. J. Exp. Med. *221*, e20231425. https://doi.org/10.1084/jem.20231425.
30. Bradley, K.C., Finsterbusch, K., Schnepf, D., Crotta, S., Llorian, M., Davidson, S., Fuchs, S.Y., Staeheli, P., and Wack, A. (2019). Microbiota-Driven Tonic Interferon Signals in Lung Stromal Cells Protect from Influenza Virus Infection. Cell Rep. *28*, 245–256.e4. https://doi.org/10.1016/j.celrep.2019.05.105.
31. Kanai, R., Nakashima, A., Doi, S., Kimura, T., Yoshida, K., Maeda, S., Ishiuchi, N., Yamada, Y., Ike, T., Doi, T., et al. (2021). Interferon-γ enhances the therapeutic effect of mesenchymal stem cells on experimental renal fibrosis. Sci. Rep. *11*, 850. https://doi.org/10.1038/s41598-020-79664-6.
32. Schroder, K., Hertzog, P.J., Ravasi, T., and Hume, D.A. (2004). Interferon-γ: an overview of signals, mechanisms and functions. J. Leukoc. Biol. *75*, 163–189. https://doi.org/10.1189/jlb.0603252.
33. Wheelock, E.F. (1965). Interferon-Like Virus-Inhibitor Induced in Human Leukocytes by Phytohemagglutinin. Science *149*, 310–311. https://doi.org/10.1126/science.149.3681.310.
34. Billiau, A., and Matthys, P. (2009). Interferon-gamma: a historical perspective. Cytokine Growth Factor Rev. *20*, 97–113. https://doi.org/10.1016/j.cytogfr.2009.02.004.
35. King, I.L., and Divangahi, M. (2019). Editorial: Evolving Mechanisms of Disease Tolerance. Front. Immunol. *10*, 2974. https://doi.org/10.3389/fimmu.2019.02974.
36. Read, A.F., Graham, A.L., and Råberg, L. (2008). Animal defenses against infectious agents: is damage control more important than pathogen control. PLoS Biol. *6*, e4. https://doi.org/10.1371/journal.pbio.1000004.
37. Powell, R.E., Soares, M.P., and Weis, S. (2023). What's new in intensive care: disease tolerance. Intensive Care Med. *49*, 1235–1237. https://doi.org/10.1007/s00134-023-07130-8.
38. Pernet, E., Downey, J., Vinh, D.C., Powell, W.S., and Divangahi, M. (2019). Leukotriene B4-type I interferon axis regulates macrophage-mediated disease tolerance to influenza infection. Nat. Microbiol. *4*, 1389–1400. https://doi.org/10.1038/s41564-019-0444-3.
39. Schieber, A.M.P., Lee, Y.M., Chang, M.W., Leblanc, M., Collins, B., Downes, M., Evans, R.M., and Ayres, J.S. (2015). Disease tolerance mediated by microbiome E. coli involves inflammasome and IGF-1 signaling. Science *350*, 558–563. https://doi.org/10.1126/science.aac6468.
40. Weis, S., Carlos, A.R., Moita, M.R., Singh, S., Blankenhaus, B., Cardoso, S., Larsen, R., Rebelo, S., Schäuble, S., Del Barrio, L., et al. (2017). Metabolic Adaptation Establishes Disease Tolerance to Sepsis. Cell *169*, 1263–1275.e14. https://doi.org/10.1016/j.cell.2017.05.031.
41. Seixas, E., Gozzelino, R., Chora, A., Ferreira, A., Silva, G., Larsen, R., Rebelo, S., Penido, C., Smith, N.R., Coutinho, A., et al. (2009). Heme oxygenase-1 affords protection against noncerebral forms of severe malaria. Proc. Natl. Acad. Sci. USA *106*, 15837–15842. https://doi.org/10.1073/pnas.0903419106.
42. Reynolds, L.A., Harcus, Y., Smith, K.A., Webb, L.M., Hewitson, J.P., Ross, E.A., Brown, S., Uematsu, S., Akira, S., Gray, D., et al. (2014). MyD88 signaling inhibits protective immunity to the gastrointestinal helminth parasite Heligmosomoides polygyrus. J. Immunol. *193*, 2984–2993. https://doi.org/10.4049/jimmunol.1401056.
43. Kapse, B., Zhang, H., Affinass, N., Ebner, F., Hartmann, S., and Rausch, S. (2022). Age-dependent rise in IFN-γ competence undermines effective type 2 responses to nematode infection. Mucosal Immunol. *15*, 1270–1282. https://doi.org/10.1038/s41385-022-00519-6.
44. Bergsbaken, T., Bevan, M.J., and Fink, P.J. (2017). Local Inflammatory Cues Regulate Differentiation and Persistence of CD8+ Tissue-Resident Memory T Cells. Cell Rep. *19*, 114–124. https://doi.org/10.1016/j.celrep.2017.03.031.
45. Knowles, C.H., Lindberg, G., Panza, E., and De Giorgio, R. (2013). New perspectives in the diagnosis and management of enteric neuropathies. Nat. Rev. Gastroenterol. Hepatol. *10*, 206–218. https://doi.org/10.1038/nrgastro.2013.18.
46. Klem, F., Wadhwa, A., Prokop, L.J., Sundt, W.J., Farrugia, G., Camilleri, M., Singh, S., and Grover, M. (2017). Prevalence, Risk Factors, and

Outcomes of Irritable Bowel Syndrome After Infectious Enteritis: A Systematic Review and Meta-analysis. Gastroenterology *152*, 1042–1054.e1. https://doi.org/10.1053/j.gastro.2016.12.039.

47. Akiho, H., Ihara, E., Motomura, Y., and Nakamura, K. (2011). Cytokine-induced alterations of gastrointestinal motility in gastrointestinal disorders. World J. Gastrointest. Pathophysiol. *2*, 72–81. https://doi.org/10.4291/wjgp.v2.i5.72.
48. Hansson, G.K., Hellstrand, M., Rymo, L., Rubbia, L., and Gabbiani, G. (1989). Interferon gamma inhibits both proliferation and expression of differentiation-specific alpha-smooth muscle actin in arterial smooth muscle cells. J. Exp. Med. *170*, 1595–1608. https://doi.org/10.1084/jem.170.5.1595.
49. Ford, C.L., Wang, Y., Morgan, K., Boktor, M., Jordan, P., Castor, T.P., and Alexander, J.S. (2019). Interferon-gamma depresses human intestinal smooth muscle cell contractility: Relevance to inflammatory gut motility disturbances. Life Sci. *222*, 69–77. https://doi.org/10.1016/j.lfs.2019.01.059.
50. Khan, W.I., Blennerhassett, P.A., Deng, Y., Gauldie, J., Vallance, B.A., and Collins, S.M. (2001). IL-12 gene transfer alters gut physiology and host immunity in nematode-infected mice. Am. J. Physiol. Gastrointest. Liver Physiol. *281*, G102–G110. https://doi.org/10.1152/ajpgi.2001.281.1.G102.
51. Zhao, A., McDermott, J., Urban, J.F., Gause, W., Madden, K.B., Yeung, K.A., Morris, S.C., Finkelman, F.D., and Shea-Donohue, T. (2003). Dependence of IL-4, IL-13, and nematode-induced alterations in murine small intestinal smooth muscle contractility on Stat6 and enteric nerves. J. Immunol. *171*, 948–954. https://doi.org/10.4049/jimmunol.171.2.948.
52. Ahrends, T., Aydin, B., Matheis, F., Classon, C.H., Marchildon, F., Furtado, G.C., Lira, S.A., and Mucida, D. (2021). Enteric pathogens induce tissue tolerance and prevent neuronal loss from subsequent infections. Cell *184*, 5715–5727.e12. https://doi.org/10.1016/j.cell.2021.10.004.
53. Sanchez-Ruiz, M., Brunn, A., Montesinos-Rongen, M., Rudroff, C., Hartmann, M., Schlüter, D., Pfitzer, G., and Deckert, M. (2019). Enteric Murine Ganglionitis Induced by Autoimmune CD8 T Cells Mimics Human Gastrointestinal Dysmotility. Am. J. Pathol. *189*, 540–551. https://doi.org/10.1016/j.ajpath.2018.11.016.
54. White, J.P., Xiong, S., Malvin, N.P., Khoury-Hanold, W., Heuckeroth, R.O., Stappenbeck, T.S., and Diamond, M.S. (2018). Intestinal Dysmotility Syndromes following Systemic Infection by Flaviviruses. Cell *175*, 1198–1212.e12. https://doi.org/10.1016/j.cell.2018.08.069.
55. Wang, H., Barry, K., Coakley, G., Moyat, M., Daunt, C.P., Zaini, A., Wickramasinghe, L.C., Yumnam, B., Camberis, M., Gros, G.L., et al. (2024). Helminth infection driven gastrointestinal hypermotility is independent of eosinophils and mediated by alterations in smooth muscle instead of enteric neurons. PLoS Pathog. *20*, e1011766. https://doi.org/10.1371/journal.ppat.1011766.
56. Sutherland, T.E., Dyer, D.P., and Allen, J.E. (2023). The extracellular matrix and the immune system: A mutually dependent relationship. Science *379*, eabp8964. https://doi.org/10.1126/science.abp8964.
57. Wang, J., Zhang, Z.-Q., Gigliotti, F., and Wright, T.W. (2023). IFN-γ Limits Immunopathogenesis but Delays Fungal Clearance during Pneumocystis Pneumonia. J. Immunol. *211*, 1397–1405. https://doi.org/10.4049/jimmunol.2300460.
58. Evaristo, C., and Alegre, M.L. (2013). IFN-γ: The Dr. Jekyll and Mr. Hyde of immunology? Am. J. Transplant. *13*, 3057–3058. https://doi.org/10.1111/ajt.12468.
59. Serger, E., Luengo-Gutierrez, L., Chadwick, J.S., Kong, G., Zhou, L., Crawford, G., Danzi, M.C., Myridakis, A., Brandis, A., Bello, A.T., et al. (2022). The gut metabolite indole-3 propionate promotes nerve regeneration and repair. Nature *607*, 585–592. https://doi.org/10.1038/s41586-022-04884-x.
60. Delacher, M., Schmidleithner, L., Simon, M., Stüve, P., Sanderink, L., Hotz-Wagenblatt, A., Wuttke, M., Schambeck, K., Ruhland, B., Hofmann, V., et al. (2024). The effector program of human CD8 T cells supports tissue remodeling. J. Exp. Med. *221*, e20230488. https://doi.org/10.1084/jem.20230488.
61. Posserud, I., Ersryd, A., and Simrén, M. (2006). Functional findings in irritable bowel syndrome. World J. Gastroenterol. *12*, 2830–2838. https://doi.org/10.3748/wjg.v12.i18.2830.
62. Saffrey, M.J. (2014). Aging of the mammalian gastrointestinal tract: a complex organ system. AGE *36*, 1019–1032. https://doi.org/10.1007/s11357-013-9603-2.
63. Pardy, R.D., Rajah, M.M., Condotta, S.A., Taylor, N.G., Sagan, S.M., and Richer, M.J. (2017). Analysis of the T Cell Response to Zika Virus and Identification of a Novel CD8+ T Cell Epitope in Immunocompetent Mice. PLoS Pathog. *13*, e1006184. https://doi.org/10.1371/journal.ppat.1006184.
64. Hapfelmeier, S., Lawson, M.A., Slack, E., Kirundi, J.K., Stoel, M., Heikenwalder, M., Cahenzli, J., Velykoredko, Y., Balmer, M.L., Endt, K., et al. (2010). Reversible microbial colonization of germ-free mice reveals the dynamics of IgA immune responses. Science *328*, 1705–1709. https://doi.org/10.1126/science.1188454.
65. Koliaraki, V., and Kollias, G. (2016). Isolation of Intestinal Mesenchymal Cells from Adult Mice. Bio-protocol *6*, e1940. https://doi.org/10.21769/BioProtoc.1940.
66. Valanparambil, R.M., Segura, M., Tam, M., Jardim, A., Geary, T.G., and Stevenson, M.M. (2014). Production and analysis of immunomodulatory excretory-secretory products from the mouse gastrointestinal nematode Heligmosomoides polygyrus bakeri. Nat. Protoc. *9*, 2740–2754. https://doi.org/10.1038/nprot.2014.184.
67. Bankhead, P., Loughrey, M.B., Fernández, J.A., Dombrowski, Y., McArt, D.G., Dunne, P.D., McQuaid, S., Gray, R.T., Murray, L.J., Coleman, H.G., et al. (2017). QuPath: Open source software for digital pathology image analysis. Sci. Rep. *7*, 16878. https://doi.org/10.1038/s41598-017-17204-5.

STAR★METHODS

KEY RESOURCES TABLE

REAGENT or RESOURCE	SOURCE	IDENTIFIER
Antibodies		
CD45.2 Pacific Blue, clone 104	eBioscience	Cat#48-0454-82; RRID: AB_11042125
CD45.2 PE, clone 104	eBioscience	Cat#12-0454-83; RRID: AB_465679
CD45.1 BV650, clone A20	Biolegend	Cat#110736; RRID: AB_2562564
CD11b BUV395, clone M1/70	BD Biosciences	Cat#563553; RRID: AB_2738276
CD11b APC Cy7, clone M1/70	eBioscience	Cat#47-0112-82; RRID: AB_1603193
NK1.1 AF700, clone PK136	eBioscience	Cat#56-5941-82; RRID: AB_2574505
Ly6G AF700, clone 1A8	Biolegend	Cat#127622; RRID: AB_10640452
CD11c PerCP Cy5.5, clone N418	eBioscience	Cat#45-0114-82; RRID: AB_925727
MHCII APC-Cy7, clone M5/114.15.2	eBioscience	Cat#47-5321-82; RRID: AB_1548783
MHCII Pacific Blue, clone M5	Invitrogen	Cat#48-5321-82; RRID: AB_1272204
Ly6C BV711, clone HK1.4	Biolegend	Cat#128037; RRID: AB_2562630
CD64 PeCy7, clone X54-5/7.1	Biolegend	Cat#139314; RRID: AB_2563903
CD3 BV650, clone BM10-37	BD Biosciences	Cat#564378; RRID: AB_2738779
TCRβ APC Cy7, clone H57-597	Invitrogen	Cat#47-5961-82; RRID: AB_1272173
CD4 PE, clone GK1.5	eBioscience	Cat#12-0041-85; RRID: AB_465508
CD4 BUV 395, clone GK1.5	BD Biosciences	Cat#563790; RRID: AB_2738426
CD8 BV605, clone 53-6.7	Biolegend	Cat#100744; RRID: AB_2561352
CD8 PeCy7, clone 53-6.7	eBioscience	Cat#25-0081-82; RRID: AB_469584
B220 FITC, clone RA3-6B2	eBioscience	Cat#11-0452-85; RRID: AB_465055
CD103 PETR, clone 2E7	eBioscience	Cat#61-1031-82; RRID: AB_2802379
CD69 PECy5, clone H1.2F3	eBioscience	Cat#15-0691-82; RRID: AB_468772
CD44 BV786, clone IM7	BD Biosciences	Cat#563736; RRID: AB_2738395
CD62L BV711, clone MEL-14	Biolegend	Cat#104445; RRID: AB_256415
PD1 PeCy7, clone J43	eBioscience	Cat#25-9985-82; RRID: AB_10853805
ICOS FITC, clone C398.4A	eBioscience	Cat#11-9949-82; RRID: AB_465458
CD49d PE, clone R1-2	Invitrogen	Cat#12-0492-82; RRID: AB_465697
CXCR3 BV650, clone CXCR3-173	Biolegend	Cat#126531; RRID: AB_2563160
EpCAM PerCP ef710, clone G8.8	eBioscience	Cat#46-5791-82; RRID: AB_10598205
Ly6A APC, clone E13-161.7	Biolegend	Cat#122512; RRID: AB_756197
α4β7 APC, clone DATK32	Invitrogen	Cat#17-5887-82**; AB_1210577**
Ki67 FITC, clone SolA15	eBioscience	Cat#11-5698-82; RRID: AB_11151330
Ki67 ef660, clone SolA15	eBioscience	Cat#50-5698-82; RRID: AB_2574235
IFNγ FITC, clone XMG1.2	eBioscience	Cat#53-7311-82; RRID: AB_469932
Gata3 PerCP ef710, clone TWAJ	eBioscience	Cat#46-9966-42; RRID: AB_10804487
Ly6G AF647, clone 1A8	Biolegend	Cat#127636; RRID: AB_2563207
CD8β PE, clone eBioH35-17.2 (H35-17.2)	eBioscience	Cat#12-0083-81; RRID: AB_657769
IL13 PE, clone eBio13A	eBioscience	Cat#12-7133-82; RRID: AB_763559
αSMA, clone EPR5368	AbCAM	Cat# ab124964; RRID: AB_11129103
RFP Antibody Pre-adsorbed	Rockland	Cat# 600-401-379; RRID: AB_2209751
Vimentin, clone EPR3776	AbCAM	Cat# ab194719; RRID: AB_2909595
E-Cadherin, clone 36	BD Biosciences	Cat#610181; RRID: AB_397580
Lectin	Sigma	Cat#L9006; RRID: AB_261832
Anti-DCAMKL1	AbCAM	Cat# ab31704; RRID: AB_873537

(*Continued on next page*)

Continued

REAGENT or RESOURCE	SOURCE	IDENTIFIER
Goat anti-Mouse AF647	Invitrogen	Cat# A21235; RRID: AB_2535804
Goat anti-Rabbit AF555	Invitrogen	Cat# A48283; RRID: AB_2896347
Donkey anti-Rat DyLight 555	Invitrogen	Cat# SA5-10027; RRID: AB_2556607
pStat1 Tyr701, clone 9167	Cell Signaling Technology	Cat#9167S; RRID: AB_3094776
Anti-mouse NK1.1, clone PK136	BioXCell	Cat# BP0036; RRID: AB_3094777
Anti-mouse Ly6G, clone 1A8	BioXCell	Cat# BE0075-1; RRID: AB_1107721
Anti-mouse IL18, clone YIGIF74-1G7	BioXCell	Cat# BE0237; RRID: AB_2687719
Anti-mouse IL15, clone M96	Amgen	Cat#M96; RRID: AB_2262243
Anti-mouse CD4, clone GK1.5	BioXCell	Cat#BE0003-1; RRID: AB_8718664
Anti-mouse CD8, clone YTS.1694	BioXCell	Cat#BE0117; RRID: AB_6533215
Anti-mouse IL-13, clone PARS-43905	Genentech	PARS-43905; RRID: N/A
Anti-mouse IL-4, clone 11B11	BioXCell	Cat#BE0045; RRID: AB_1107707
Anti-LIX, clone 61905	R&D Biosystems	Cat#MAB433-500; RRID: 2086587
Rat IgG2b, isotype control	BioXcell	Cat#BP0085; RRID: AB_3094778
Anti-mouse IgG2a, clone C1.18.4	BioXCell	Cat#C1.18.4; RRID: AB_4758199
Envison+ Single Reagent (HRP.Rabbit)	Agilent	Cat#K400311-2
Bacterial and virus strains		
Lymphocytic Choriomeningitis Virus (LCMV)	Pardy et al.[63] Plos Pathogens	Provided by Martin Richer
E. coli, strain HA107	Hapfelmeier et al.[64]	Donated by Andrew McPherson
Chemicals, peptides, and recombinant proteins		
FTY720	Sigma	Cat#SML0700
SB431542	Sigma	Cat#S4317-5MG
Viability dye, ef660	Invitrogen	Cat#65-0866-14
Contour next Blood Glucose Test Strips	Ascensia Diabetes Care	N/A
Carmine Red	Sigma	Cat#C1022
Recombinant Mouse IFNγ	Peprotech	Cat#315-05
Recombinant Murine IL2	Peprotech	Cat# 212-12
Recombinant Murine IL12	Peprotech	Cat# 210-12
Recombinant Mouse IL18	Biolegend	Cat# 767004
Recombinant Murine IL33	Peprotech	Cat#:210-33
Recombinant Mouse IL36g	Biolegend	Cat# 552802
TRITC-Dextran	Sigma	Cat#T1037
FITC-Dextran	Sigma	Cat#FD4
Collagenase VIII	Sigma	Cat#C2139
Collagenase XI	Sigma	Cat#C7657-100MG
Dispase II	Sigma	Cat#D4693-1G
DNase II	Sigma	Cat#D8764-30KU
DNase I	Sigma	Cat#D5025-375KU
Tri-reagent	Sigma	Cat#T9424-200ML
GolgiStop	BD Bioscience	Cat#554724
3,3'-Diaminobenzidine (DAB) reagent	Sigma	Cat#D3939
Cxcl5 RNAScope Probe	ACDBio	Cat#467441
Prolong diamond antifade mountant	Invitrogen	Cat#P36970
Epredia™ Cytoseal™ Mountant; 60, 280 and XYL	ThermoFisher	Cat#:23-243-256
Defibrinated Sheep Blood	Hardy Diagnostics	Cat#DSB500
Tamoxifen	Sigma	Cat#T5648
Hematoxylin	Sigma	Cat#MHS16-500mL
Eosin	Sigma	Cat# HT110116-500mL

(*Continued on next page*)

Continued

REAGENT or RESOURCE	SOURCE	IDENTIFIER
Critical commercial assays		
RNAScope 2.5HD Detection Reagents	ACDBio	Cat#322310
RNAScope Multiplex Fluorescent V2	ACDBio	Cat#UM323100
Foxp3 Fixation/Permeabilization Kit	Invitrogen	Cat#00-5123-43
Advance Tech QPCR Mix	Advantech	Cat#AD100-21 402
AdvanTech 5x Reverse Transcription Mastermix	Advantech	Cat#AD100-31404
EasySep Stem CD8 T Cell Isolation Kit	Stem Cell Technologies	Cat#19853C.1
EasySep Mouse T Cell isolation kit	Stem Cell Technologies	Cat#19851
Experimental models: Cell lines		
HEK-Blue mTLR4 cells	InvivoGen	Cat#hkb-mtlr4
Experimental models: Organisms/strains		
Parasite: Heligomosomoides polygyrus bakeri	In house	Gentile et al.[6]
Mouse: C57BL/6	Charles River	Cat#027
Mouse: NCI B6-Ly5.1	Charles River	Cat#564
Mouse: Ifng$^{-/-}$	The Jackson Laboratories	Cat#002287
Mouse: GREAT	The Jackson Laboratories	Cat#017581
Mouse: Myd88$^{fl/fl}$	The Jackson Laboratories	Cat#009108
Mouse: Ccr2$^{-/-}$	The Jackson Laboratories	Cat#017586
Mouse: Ifngr$^{-/-}$	The Jackson Laboratories	Cat#003288
Mouse: Ifngr$^{fl/fl}$	The Jackson Laboratories	Cat#025394
Mouse: Germ Free Mouse	International Microbiome Centre at the University of Calgary	N/A
Mouse: OT-1 Rag$^{-/-}$ Ly5.1	Heather Melichar	N/A
Mouse: Rag1$^{-/-}$	Jackson	Cat#002216
Mouse: TCRβ-/-	Judith Mandl	N/A
Mouse: CreERT2	Joaquin Madrenas, The Jackson Laboratories	Cat#008463
Mouse: Myh11Ert2-cre	The Jackson Laboratories	Cat#019079
Mouse: Col1A2-cre	Alex Gregorieff	N/A
Mouse: Villin-cre	The Jackson Laboratories	Cat#004586
Mouse: IL33$^{-/-}$	Herbert De'Broski	N/A
Mouse: E8i-cre x *Il36r*$^{-/-}$	Oliver Harrison	N/A
Oligonucleotides		
Ifng F: TTCTTCAGCAACAGCAAGGC	This Paper	N/A
Ifng R: ACTCCTTTTCCGCTTCCTGA	This Paper	N/A
Cxcl9 F: CTTTTCCTCTTGGGCATCAT	This Paper	N/A
Cxcl9 R: GCATCGTGCATTCCTTATCA	This Paper	N/A
Cxcl10 F: GCACCATGAACCCAAGTG	This Paper	N/A
Cxcl10 R: TTCATCGTGGCAATGATCTCAACA	This Paper	N/A
Ly6a F: GGAGGCAGCAGTTATTGTGG	This Paper	N/A
Ly6a R: GCTACATTGCAGAGGTCTTCC	This Paper	N/A
Il18 F: CAAGCATCCAGGCACAGC	This Paper	N/A
Il18 R: CTGATGCTGGAGGTTGCAGA	This Paper	N/A
Il33 F: ATCCTTGCTTGGCAGTATCC	This Paper	N/A
Il33 R: AGCTGGTTGTCCTTCACTCC	This Paper	N/A
Il36g F: ATGGACACCCTACTTTGCTG	This Paper	N/A
ILl36g R: TGTCCGGGTGTGGTAAAACA	This Paper	N/A
Hprt F: AGGACCTCTCGAAGTGTTGG	This Paper	N/A

(*Continued on next page*)

Continued

REAGENT or RESOURCE	SOURCE	IDENTIFIER
Hprt R: AACTTGCGCTCATCTTAGGC	This Paper	N/A
Cxcl1 F: CCAGAGCTTGAAGGTGTTGC	This Paper	N/A
Cxcl1 R: CAGACAGGTGCCATCAGAGC	This Paper	N/A
Cxcl2 F: TCCAGAGCTTGAGTGTGACG	This Paper	N/A
Cxcl2 R: TCCAGGTCAGTTAGCCTTGC	This Paper	N/A
Cxcl5 F: CCATCTCGCCATTCATGC	This Paper	N/A
Cxcl5 R: AGCTATGACTTCCACCGTAGG	This Paper	N/A
Ccl2 F: GCTCAAGAGAGAGGTCTGTGC	This Paper	N/A
Ccl2 R: GTGCTTGAGGTGGTTGTGG	This Paper	N/A
Ccl3 F: GCCCTTGCTGTTCTTCTC	This Paper	N/A
Ccl3 R: GGCAATCAGTTCCAGGTC	This Paper	N/A
Ym1 F: CAGTGCCATGGTCTCTACTCC	This Paper	N/A
Ym1 R: AATGATTCCTGCTCCTGTGG	This Paper	N/A
Arg1 F: TGATGGAAGAGACCTTCAGC	This Paper	N/A
Arg1 R: CACCTCCTCTGCTGTCTTCC	This Paper	N/A
Software and algorithms		
Flow Jo v10	BD Biosciences	https://www.flowjo.com
FACSDiva v9.0	BD Biosciences	https://www.bdbiosciences.com/en-ca/products/software/instrument-software/bd-facsdiva-software
Prism v10	Graphpad Software	https://www.graphpad.com/features
Image J	National Institute of Health (NIH)	https://wsr.imagej.net/notes.html
Biorender	N/A	Biorender.com
Zen Microscopy Software	Zeiss	https://www.zeiss.com/microscopy/en/products/software/zeiss-zen.html
QuPath	QuPath	https://qupath.github.io
clusterProfiler	Bioconductor	https://doi.org/10.18129/B9.bioc.clusterProfiler
enrichplot	Bioconductor	https://doi.org/10.18129/B9.bioc.enrichplot

EXPERIMENTAL MODEL AND STUDY PARTICIPANT DETAILS

Mice

All experimental procedures were performed in accordance with the McGill University Health Centre Research Institute Animal Resource Division with approved use protocol #7977. All mice were used between 6-10 weeks of age with an average weight of 18-25g. Wildtype (C57BL/6, No. 027) and CD45.1 (NCI B6-Ly5.1, No. 564) were obtained from Charles River. Ifng$^{-/-}$ (No. 002287), GREAT (No. 017581), *Myd88*$^{fl/fl}$ (No. 009108), *Ifngr* $^{-/-}$ mice (No. 003288), *Ccr2* $^{-/-}$ mice (No. 017586), *Ifngr* $^{fl/fl}$ (No. 025394), *Villin*-cre (No. 004586), *Myh11Ert2*-cre (No. 019079), R26ERT2cre mice (No. 008463) and Col1A2Ert2-cre were all obtained from Jackson Labs. Germ free mice on a B6 background were purchased from the International Microbiome Centre at the University of Calgary. OT-I x Rag$^{-/-}$ Ly5.1 were bred and maintained at our institution while TCRβKO mice were provided by Judith Mandl (McGill). IL-33$^{-/-}$ mice and E8icre-Il36r$^{fl/fl}$ mice were bred and maintained at the University of Pennsylvania and Benaroya Institute, respectively. All mice were backcrossed to the C57BL/6 background and transgenic lines were bred in house. Mice were housed in groups (4-5 mice per cage) with *ad libidum* access to standard chow and water. Animals were housed at 22C with a 12h cycle of lights on (7am) and lights off (7pm). For all transgenic mice, littermates of the same sex were randomly assigned to experimental groups. For WT and germline transgenic models, mice of the same sex and age were randomly assigned to experimental groups. Sex had no effect on the experimental outputs, so all combined data is expressed as a combination of the sexes. Experiments involving germline gene-deficient mice were conducted at least once in adults co-housed (female mice) or mixed bedding (male mice) for at least three weeks prior to experimentation to normalize microbiome effects. Uninfected and infected mice were not co-housed during an experiment. Health of the mice was monitored every 2-3 days or daily, in the case of high dose infection studies. Any mouse that reached a body score of 2 or lost more than 20% of their initial weight was euthanized as a humane endpoint.

Cell lines

The mouse TLR4 reporter HEK293 cells (HEK-Blue mTLR4 cells) were engineered from the human embryonic kidney HEK293 cell line. Cells were used below 10 passages at 70-80% confluency and maintained at 37C with 5% CO_2. Source details can be found in the key resources table. Primary fibroblast cultures were generated from the top 10 cm of the small intestine as previously described.[65] Briefly, the intestine was washed with antibiotics and the epithelial layer removed with a EDTA (5mM) and DTT (1mM) solution for 30 min at 37C. Fibroblasts were liberated in a digestion media composed of collagenase XI (300U/mL), dispase II (0.08 U/mL) and DNase II (50U/mL), for 20 min at 37C. Fibroblasts were filtered, pelleted and resuspended in fibroblast media (DMEM, 10 % FBS, penicillin/streptomycin, glutamine and non-essential amino acids). After 3 h, the media with non-attached cells was aspirated and the adherent cells were defined as fibroblasts. Cultures were passaged three times before experiments were conducted. Replicates were completed from both male and female mice and there was no association between sex and experimental output.

Parasite

Heligmosomoides polygyrus bakeri is maintained in house.

METHOD DETAILS

Helminth infection and tamoxifen treatment

Infectious L3 larvae were propagated from specific pathogen free (SPF) feces according to standard practices.[66] Briefly, feces were collected in empty cages from adult mice infected with 200 L3 larvae at 2-12 weeks post infection. The feces was moistened in water and placed on double-lined whatman paper inside a cell culture dish. The fecal-egg mixture was moistened every 3-4 days and after 10 days, the larvae were harvested by washing the whatman paper in sterile water. Collected larvae were counted, at kept at 4C until use. Viability and concentration of larvae were validated before every infection. Unless indicated, mice were infected with 200 L3 larvae by oral gavage in sterile water. For high dose infection studies, mice were gavaged with 600 L3 larvae in sterile water. For inducible promoters, mice were gavaged with 5 mg of tamoxifen (Sigma Cat#T5648) dissolved in a 9:1 mixture of corn oil and ethanol. Treatments were delivered on days -7 and -6 days before infection.

Antibody treatment

FTY720 experiments were conducted by treating mice intraperitoneally (i.p.) with 1 μg/g of body weight of FTY720 in sterile water starting 4 days before infection and every other day until sacrifice. For NK cell depletion experiments, mice were treated i.p. with 200 μg of anti-NK1.1 depletion antibody (clone PK136, BioXcell) or isotype (clone C1.18.4, BioXcell) on the day before infection and every second day until sacrifice.[6] Neutrophils were depleted with an αLy6G antibody (clone BE0075-1, BioXCell) with a dose of 200 μg i.p. at days -1 and alternating until sacrifice. Neutrophil depletion was verified with Gr-1 staining in blood and tissue. CD4 (BioXCell, clone GK1.5) and CD8 (BioXCell, clone YTS.1694) T cells were depleted using 250 μg and 200 μg i.p. of neutralizing antibodies, respectively, 1 day before infection. IL-18 was depleted using the anti-IL18 antibody (BioXCell, clone YIGIF74-1G7), at a dose of i.p. 200 μg per mouse starting 1 day before infection and every other day until sacrifice. IL-15 was similarly neutralized using i.p. 200 μg of the M96 clone with the IgG2a (clone C1.18.4) as a control. CXCL5 (clone 61905) was neutralized with a dose of 30 μg, the day before, and every second day until sacrifice. Type 2 cytokines were eliminated using 500μg each of anti-IL4 (clone BE0045) and IL13 (clone PARS-43905) 1 day before infection. For the high dose infections lasting until 8 dpi, a second dose was given 4 days after infection.

Small molecule treatment experiments

TRITC-Dextran (Sigma Cat#T1037) was administered intravascularly at 50 mg/kg in sterile physiological saline 10 min before sacrifice. Tissue for histology was prepared as described for immunofluorescence below. FITC-Dextran (Sigma Cat#FD4) was administered to 3 h fasted mice at a dose of 12 mg in 150 μl of PBS by oral gavage. Food was replaced and mice were sacrificed 4 h later by cardiac puncture. Plasma was isolated and FITC signal was read immediately on a Tecan infinite M200 plate reader. Dosing of rIFNγ was conducted by i.p. treatment with 1 μg of rIFNγ (Peprotech, Cat#315-05) daily from the day of infection until the day of sacrifice. To validate the IL-18 neutralization approach, mice were treated with the anti-IL18 neutralization antibody as described above 1 day before IL-12p70 (250ng) and IL-18 (750ng) by i.p. injection on day 0 and 1, before sacrifice on the third day.

Adoptive transfer experiments

For the adoptive transfer of WT and Ifng$^{-/-}$ T cells into TCRβ$^{-/-}$ mice, T cells from the spleen and lymph nodes were isolated using Stem cell EasySep Mouse T Cell isolation kit (Cat#19851) and a total of 5 million cells were transferred to recipient TCRβKO mice. For the adoptive transfer of OT-1xRag1$^{-/-}$ cells into Rag1$^{-/-}$ mice, whole spleens from OT-1 Rag1$^{-/-}$ mice were isolated and 5 million cells were transferred to CD45.2 Rag1$^{-/-}$ mice. For the controls, CD8 T cells were isolated from the spleens of CD45.2 WT mice using the EasySep Stem Cell Kit for CD8 T cells (Cat#19853C.1) and 5 million cells were transferred into CD45.2 Rag1$^{-/-}$ mice. P14 cell adoptive transfer and LCMV infection was conducted as previously described.[63] Thy1.2 CD8^{+} TCR transgenic cells (P14 cells, specific to

GP_{33-41} of LCMV) were i.v. injected into WT Thy1.1 C57BL/6 recipient mice. After 1 day, mice were infected (i.p.) with 2×10^5 PFU of LCMV Armstrong. Mice were allowed to rest for 6 weeks to clear the infection and rechallenged with 200L3 *Hpb* larvae.

Bone marrow chimeras

Recipient mice were irradiated (X-RAD SmART Irradiator) twice, 4 h apart with 5.5 Gy of irradiation for a final lethal dose of 11 Gy. 1-2 mice were kept as sentinels to verify lethal dose of irradiation was given. Immediately after the second dose, mice were i.v. injected with total bone marrow cells from donor mice with 5 million cells/mouse. Mice were allowed to reach chimerism for 8 weeks before infection with *Hpb*.

Germ free mice experiments

Fecal microbiota transfers (FMT) were performed by taking SPF feces from sex-matched adult WT mice and diluting 160 times in sterile reduced PBS. The slurry was filtered through 100 μm mesh filters and 250 μL was gavaged into germ free (GF) mice. Mice were allowed to conventionalize for 3 weeks before infection. GF larvae were prepared from adult SPF mice as previously described.[19] Adult worms were collected from SPF mice at 2-3 weeks post-nfection and placed in an antibiotic bath. After 18h, the worms and eggs were collected and worms were filtered out through a 100 μm filter and eggs were pelleted by centrifugation. The eggs were incubated at 4°C for 24 hours with a high concentration of antibiotics. The sterilized eggs were washed several times in sterile PBS, counted and mixed with aucotrophic *E. coli* HA107. The egg-bacteria mixture was placed on a nutrient agar and eggs were allowed to hatch for 5 days. Eggs were collected in sterile water, washed several time in sterile water and the number of viable, sterile *Hpb* larvae were counted. After preforming sterility verification on bacterial and fungal plates, the larval preparation was given to GF or conventionalized mice. Both GF and conventionalized mice were infected with sterile *Hpb* larvae as described above.

Granuloma characterization

Where possible, and indicated, the researchers were blinded to the experimental groups. The top 5-10 cm of the proximal duodenum was harvested and placed in sterile HBSS supplemented with 5 % FBS. Intestines were cut longitudinally and under a Micromaster dissection microscope (Fisher scientific) at 4X zoom, visible granulomas were counted and scored for their hemorrhagic nature. The granuloma diameter was measured using an electric caliper (Electronix Digital Caliper, IP54) and each point is representative of the average size of 20-30 granulomas found within the tissue processed.

For the blinded assay, 2 researchers were blinded to the experimental groups and agreed upon a hemorrhagic rubric. "Hemo1" was designated a damaged granuloma whose bleeding did not extend beyond the bounds of the active granuloma whereas "Hemo2" was more extensive damage where the damage extended beyond the confines of the granuloma.

Carmine red transit time assay

Unfasted mice were orally gavaged with 200μL of 6% carmine red, prepared in PBS, within 2 h of the facility's lights on. Fecal pellets were monitored continuously until the first pellet with a full red color was passed by each mouse while the time for the first pellet to emerge was considered to be transit time.

Cell Extraction and flow cytometry

The proximal 5-10cm of the duodenum was used to extract lamina propria (LP) or intestinal epithelial cells (IECs) as previously described.[6] In brief, fat and peyer's patches were removed from the tissue and subsequently washed in Hank's Balanced Salt Solution (HBSS) before two 20 min incubations at 37°C in 5mM EDTA buffer in HBSS supplemented with 10% heat inactivated fetal bovine serum (FBS) and 15mM HEPES. The tissue was filtered through a 100 μm filter to collect the IEC compartment. The remaining tissue was washed twice in HBSS with 10% FBS and digested in RPMI 1640 supplemented with 10% FBS, 15mM HEPES, 100U/mL of DNase and 200 U/mL of collagenase VIII for 23 min at 37°C with shaking at 250rpm. The digestion was stopped by adding 35 mL of cold R10 buffer (RPMI 1640 supplemented with 10% FBS, 15mM HEPES, 1% L-glutamine and 1% penicillin/streptomycin). The tissue was manually crushed, passed through a 100 μm filter and centrifuged at 1800 rpm for 8 min at 4°C and resuspended in R10 buffer. For experiments where cells were stimulated, 3 million cells were washed twice in sterile PBS μ resuspending them in PMA (100 nM), ionomycin (1 μm) and GolgiStop (0.67uL/mL) for 4h at 37°C. The cell suspension was incubated with a fixable viability dye (eFluor 506) for 20 min at 4°C. Cells were washed and incubated with Fc block (10 min at 4°C) following be surface staining (30 min at 4°C). Cells were fixed and permeabilized with the FoxP3 Fix/Perm kit for 30 min at 4°C according to manufacturer's instructions and intercellular staining was performed in the kit's permeabilization buffer (45 min at 4°C). Data acquisition was performed with a LSR Fortessa (BD Biosciences) and analyzed using FlowJo software (BD Biosciences).

Immunofluorescence

Stainings for αSMA, neutrophils and goblet/tuft cells were conducted on formalin-fixed paraffin-embedded tissues (FFPE). Freshly dissected tissues were cut longitudinally, washed in cold PBS, immediately prepared into a "Swiss roll" and placed in a histological cassette. Tissue was fixed in 10 % formalin for 24 h before being rinsed and transferred to 70 % ethanol. Sections were paraffin embedded by the histological core at the RI-MUHC and cut into 5 μm section using a microtome (Leica). Sections were deparaffinized in sequential xylene washes followed by serial hydration steps in descending concentrations of ethanol. Antigen retrieval was

done in citrate buffer for 20 min in a steamer followed by rest in the hot citrate buffer for 20 min at room temperature. Slides were washed 3 times for 5 min in PBS before blocking with 3% bovine serum albumin (BSA) in PBS for 3 h. Samples were left with the primary antibody (indicated in key resources table) for 24 h at 4 °C followed by a secondary antibody stain (indicated in key resources table) for 2 h at room temperature in a hydration chamber. Slides were mounted in Prolong diamond antifade mountant (Invitrogen, Cat#P36970) and allowed to cure at room temperature overnight before imaging on Zeiss confocal microscope (LSM700). Images analysis was done in ImageJ (NIH) and in QuPath.[67] Enumeration of neutrophils within the granuloma was done manually and represented as the number of neutrophils per granuloma area determined using an automated function of QuPath. αSMA quantification was conducted in ImageJ (NIH) as the number of positive αSMA pixels per granuloma associated region, including the affiliated villi. Quantification of the number of goblet and tuft cells was determined manually, compared to an automatically selected outline of villi regions in the granuloma associated regions using an automatic function in Qupath. For all immunofluorescent quantifications, an average of 4-5 granuloma regions per mouse were averaged to represent the enumeration for 1 mouse.

Staining for CD8 T cells was conducted on fresh-frozen tissue sections. Swiss rolls were prepared as described above but were embedded in OCT in plastic cassettes and frozen slowly in liquid nitrogen vapour. Samples were cut on a cryostat to 6μm thickness and fixed in an ice cold ethanol-acetone 75:25 v/v mixture for 10 min at room temperature. Slides were washed 3 x 5 min in PBS and blocked in 3% BSA with Fc block. Unconjugated CD8 primary antibodies were added (see key resources table) for 2h at room temperature before being transferred to 4°C overnight. Slides were washed 3 x 5 min in PBS and incubated with secondary antibody for 2 h at room temperature. Slides were washed again, stained with DAPI for 10 min at room temperature, washed again and mounted in Prolong antifade mountant as described above.

Immunohistochemistry

Slides were prepared as described for immunofluorescence. Slides were deparaffinized and rehydrated in several gradients of descending ethanol. Antigen retrieval was performed for 20 min at >90°C in pre-warmed citrate buffer in a steamer. Samples were allowed to rest in the citrate buffer for 20 min outside of the steamer followed by quenching in 3 % hydrogen peroxide for 15 min and one 10 min wash in PBS. Samples were blocked in 1 % BSA in PBS for 3 h in a hydration chamber followed by primary antibody staining with pStat1 (Tyr701, Cell Signaling #9167) at 1:200 dilution overnight at 4 °C. After 3, 20 min washes in PBS, a secondary antibody stain with a ready-mix rabbit HRP antibody (Dako Cat#K4003) was performed for 90 min at room temperature. After 3, 20 min washes in PBS, staining was revealed with 3,3'-Diaminobenzidine (DAB) reagent (Sigma Cat#D3939) according to manufacturer's instructions. Images were further counterstained with hemoxylin, followed by bluing in acidified water and dehydration and clearing in xylene. Slides were mounted in a xylene-based mountant (Cytoseal; Thermofisher) and imaged on an Axio Imager M2 microscope (Zeiss) with 20X magnification.

H&E Staining

Formalin-fixed paraffin-embedded blocks were cut to 5μm on a microtome, as described for immunofluorescence. After drying, slides were hydrated by 3x3 min washes in xylene, 3x3 min in ethanol and 1 min in 95% ethanol. Slides were placed in Mayer's hematoxylin for 10 min followed by washing and blueing in an acidic bath. Eosin counterstain was done for 30 sec followed by 2x2 min washes in 90% ethanol and 3x2 min washes in xylene. Slides were mounted in a xylene-based mountant (Cytoseal; Thermofisher) and imaged on an Axio Imager M2 microscope (Zeiss) with 20X magnification.

RNAScope

RNAScope was performed according to manufacturer instructions (ACD bio, Cat#322310) using the RNAscope probe *Cxcl5* (Cat#467441). Images were acquired with an Axio Imager M2 microscope (Zeiss) at 20X magnification. Images were quantified using the pixel count function of Qupath, a digital pathology image analysis software.[67]

Co-staining of *Cxcl5* (RNAScope) with immunofluorescence of a TdTomato tag was conducted using the Multiplex flurescent reagent kit v2 (RNAScope, UM323100), according to manufacturer's instructions and following the immunofluorescent staining protocol as described above.

RNA extraction and qPCR

RNA was extracted from 0.5 cm of tissue using Tri reagent (Sigma-Aldrich) following manufacturer's instructions, with an additional overnight ethanol precipitation step. Briefly, cleaned RNA was resuspended in 90 μl of water with 10 μl of 3M ammonium acetate and combined with 300 μl of ice cold ethanol and left at -20°C for 18 h. Purified RNA was centrifuged, washed in 70% ethanol and resuspended in a final volume of RNase/DNase-free water. Reverse transcript was performed with AdvanTech 5x Reverse Transcription Mastermix (Cat# AD100-31404) and quantitative PCR was conducted using Advance Tech QPCR Mix (Advantech, Cat# AD100-21 402) and analyzed relative to HPRT internal controls using the $2^{-\Delta\Delta CT}$ method. All primer pairs are listed in the key resources table.

Ex vivo stimulation

Small intestinal cell preparations were made according to the protocol for FACS. Single cells were placed in a 24 well plate at 3 x 10^6 cells in T cell media containing RPMI, 10% FBS, penicillin/streptomycin and 5mM HEPES. Cells were stimulated with a combination of IL-2 (0.55 ng/mL), IL-12 (10 ng/mL), IL-33 (25 ng/mL), IL-18 (10 ng/mL) and/or IL-36g (10 ng/mL) for 18 h at 37 °C). 4 h before the end of the stimulation, GolgiStop was added to the preparation.

Fibroblast stimulation

Once at confluency, primary fibroblasts were split into 24 well plates and allowed to grow for 24h. Following, cells were washed twice in PBS and media was replaced with a starvation media (DMEM, 0.1% BSA, pen/strep, glutamine and non-essential amino acids) for 16h. Cells were stimulated by replacing media with fresh starvation media with 5 ng/mL of rIFNγ. Cells were harvested in Trizol at the appropriate time point.

Granuloma biopsies

Mice were sacrificed one at a time and intestines were placed in cold HBSS + 10% FBS. Intestines were immediate cut longitudinally and placed epithelial side up behind a dissection microscope in a cold room. Biopsies of granuloma and non-granuloma regions were made with a circular biopsy punch (3mm) and immediately frozen in liquid nitrogen.

Tissue Bacterial Burden

Systemic bacterial burden was determined by taking whole tissue slurries of the lung, liver and spleen prepared by manually crushing the tissue through a 100 μm filter. The suspension was made up to 5 ml and 100 μl of this solution, or its dilutions, was plated on TSA plates with 5 % defibrillated sheep's blood. The TSA base was composed of 10 g of Peptone, 10 g of yeast, 5 g of NaCl and 15 g agar per liter of water. Plates were incubated aerobically for 48 h before enumeration of colonies manually.

Serology

Plasma was stored at -80°C until further analysis. Measurements of conventional serological parameters were performed by SYN-LAB.vet GmbH (Leipzig, Germany).

Cytokine measurements

Plasma cytokines were determined in duplicates using the LEGENDplex™ Mouse Inflammation Panel 13-plex (BioLegend, San Diego) on a BD Accuri™ C6 Plus Flow Cytometer (BD Biosciences) according to manufacturer instructions.

QUANTIFICATION AND STATISTICAL ANALYSIS

Bulk RNA seq analysis

Reanalysis of the RNASeq dataset was conducted in R using ClusterProfiler and DOSE R packages. Code is available in the supplemental information.

Statistical analysis

Details of the statistical analyses in terms of group sizes and specific tests used can be found in the figure legends. All data are represented at the mean results derived from independent mice with the spread of data represented as the standard error of the mean (SEM) with significance determined when $p < 0.05$. GraphPad Prism 10 software was used to perform statistical analyses. Student's t test, one- or two-way ANOVA were used as appropriate. Nonparametric tests were used when the results did not fit a normal distribution.

GSEA analysis raw code

Load required packages

```{r, message=F, warning=F}

library(tidyverse)
library(magrittr)
library(clusterProfiler)
library(enrichplot)
library(ggrepel)

# Set organism to mouse
```{r, message=F, warning=F}
organism <- "org.Mm.eg.db"
library(organism, character.only = TRUE)
```
```

Prepare data
```{r}
#load deseq of bulk small intestine RNAseq uninfected vs 2 dpi of Hpb
df <- read_csv("Constrast3.uninf.vs.day2.csv")
#Create a vector of the log2 fold changes
original_gene_list <- df$log_FC
#Add ENSEMBL IDs as names to the vector
names(original_gene_list) <- df$id
#Remove NAs
gene_list<-na.omit(original_gene_list)
#Sort the vector by decrease log2 fold change
gene_list = sort(gene_list, decreasing = TRUE)
# GSE
```{r}
#Perform the gene set enrichment using biology process terms
gse <- gseGO(geneList=gene_list,
ont ="BP",
keyType = "ENSEMBL",
pvalueCutoff = 0.05,
nPermSimple = 10000,
verbose = TRUE,
minGSSize = 10,
maxGSSize = 500,
OrgDb = organism,
pAdjustMethod = "none",
eps = 0)
# Dotplot
```{r, fig.height= 9}
require(DOSE)
dotplot(gse, showCategory=20)+
coord_fixed(ratio = 0.01)
# Export GSE results
```{r}
write.csv(gse@result, "GSEA_results.csv", row.names=FALSE)
# Print GSEA plots
```{r, fig.height=6}
#GO:1990266
gseaplot(gse, by = "all", title = gse$Description[16], geneSetID = 16, line_width = 16)
```{r, fig.height=6}
#GO:0030593
gseaplot(gse, by = "all", title = gse$Description[19], geneSetID = 19)
```{r, fig.height=6}
#GO:0002274
gseaplot(gse, by = "all", title = gse$Description[60], geneSetID = 60)
```{r, fig.height=6}

```
#GO:0090594
gseaplot(gse, by = "all", title = gse$Description[306], geneSetID = 306)
```{r, fig.height=6}
#GO:0042060
gseaplot(gse, by = "all", title = gse$Description[311], geneSetID = 311)
```{r, fig.height=6}
#GO:0032609
gseaplot(gse, by = "all", title = gse$Description[312], geneSetID = 312)
# Print enrichment map
```{r echo=TRUE}
emapplot(pairwise_termsim(gse), showCategory = 50, cex_category = 0.5, cex_line = 0.5, cex_label_category = 0.75)
```
```

Supplemental figures

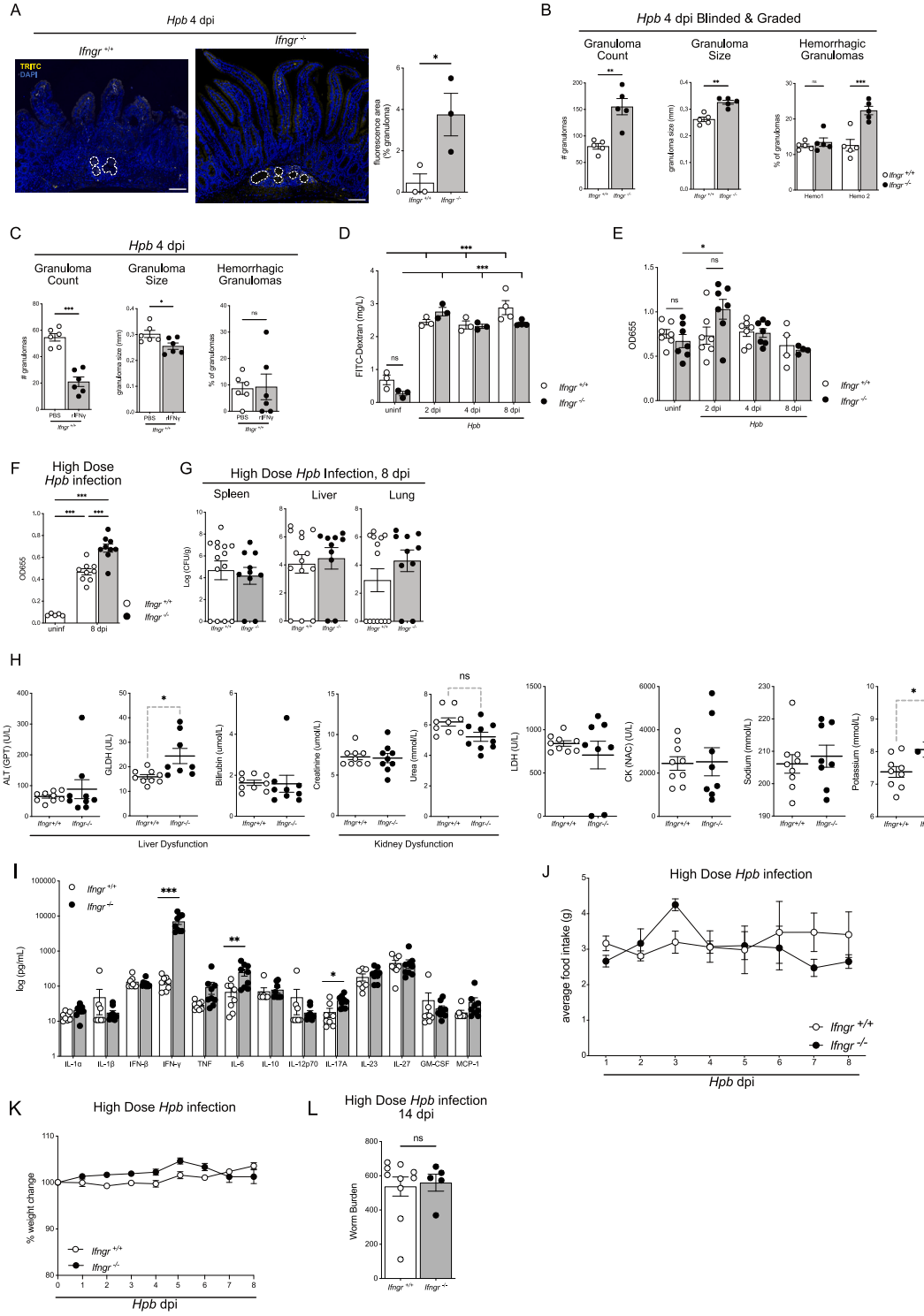

(legend on next page)

Figure S1. Local and systemic measures of morbidity during early *Hpb* infection, related to Figure 1

(A) TRITC-dextran dye was administered intravenously to 4-day *Hpb*-infected mice 10 min before sacrifice. Representative immunofluorescent images of Ifngr$^{+/+}$ and Ifngr$^{-/-}$ mice showing TRITC infiltration (yellow) into the granuloma (left) with quantification (right). Quantification represents the fraction of fluorescent area with a TRITC-positive signal normalized to the total area of the granulomatous area. Scale bar, 50 μm; one experiment, n = 3 mice per group.

(B) Repeated counting, sizing, and scoring of hemorrhagic granulomas of Ifngr$^{+/+}$ and Ifngr$^{-/-}$ mice by two blinded investigators (refer to Figure 1E). Hemo1 corresponds to low-grade hemorrhaging within the granuloma area, and Hemo2 indicates high-grade hemorrhaging extending into nearby tissue areas.

(C) Granuloma characterization following daily low-dose recombinant IFNγ (rIFNγ) treatment of Ifngr$^{+/+}$ mice until the time of sacrifice. Two pooled independent experiments, n = 6 mice per group.

(D) FITC-dextran test of intestinal permeability following *Hpb* infection at various time points. One experiment, n = 3 mice per group.

(E) Indirect endotoxin measurement from *Hpb*-infected mice from plasma using TLR4-HEK-Blue cell reporter line. Semi-quantitative data are represented as the OD655 from the cell supernatant. Two independent pooled experiments, n = 7 mice per group.

(F) Circulating endotoxin levels as a proxy for intestinal permeability in high-dose *Hpb*-infected mice were measured semi-quantitatively with TLR4-HEK-Blue reporter cells represented as raw OD655 levels.

(G) Total aerobically culturable bacterial burden from high-dose infected mice at day 8 post high-dose *Hpb* infection in the whole spleen, liver, and lung normalized to the weight of tissue harvested. Three pooled independent experiments, n = 10–14 mice per group.

(H) Serology report from high-dose *Hpb*-infected mice at day 8.

(I) Cytokine profile of the same groups shown in C. Serology and cytokines conducted using n = 9–10 mice per group.

(J) Daily average food intake of 2 mice (3 cages of 2 mice per cage; total n of 6) following high-dose infection.

(K) Weight change of Ifngr$^{+/+}$ and Ifngr$^{-/-}$ mice following high-dose infection measured as the percent change from initial weight on day 0; pooled data from two independent experiments, 5 mice per group. (L) Worm burden at 14 dpi of surviving mice following high-dose infection in Ifngr$^{+/+}$ and Ifngr$^{-/-}$ mice. Two independent pooled experiments, n = 5–10 per group. ALT, alanine transaminase; GLDH, glutamate dehydrogenase; LDH, lactate dehydrogenase; CK, creatine kinase. Each dot represents an individual mouse. Between-group comparisons were analyzed with nonparametric Student's t test and time course analyses' significance with two-way ANOVA. $^{*}p < 0.05$, $^{**}p < 0.01$, $^{***}p < 0.001$; ns, not significant.

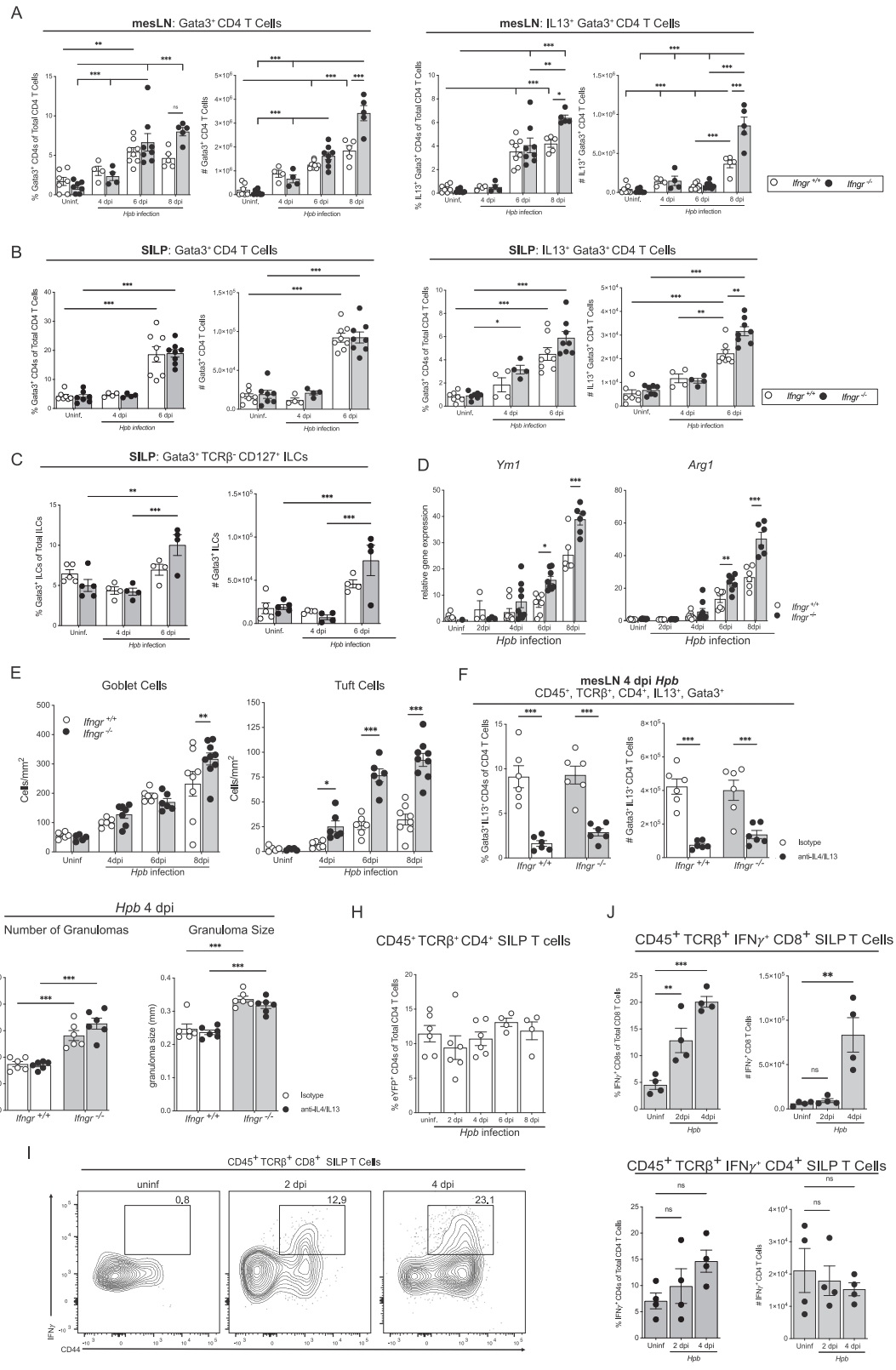

(legend on next page)

Figure S2. Characterization of type 1 and type 2 immune responses during early *Hpb* infection, related to Figures 1 and 2

(A and B) Type 2 immune profiling of Gata3$^+$ IL13$^+$ CD4$^+$ T cells from the mesenteric lymph nodes (mesLN) (A) and SILP (B) of *Hpb*-infected Ifngr$^{+/+}$ and Ifngr$^{-/-}$ mice following *ex vivo* PMA/ionomycin stimulation. The frequency of Gata3$^+$ CD4 T cells and Gata3$^+$ IL13$^+$ CD4$^+$ T cells is represented as the frequency of total CD4$^+$ T cells.

(C) Frequency and number of Gata3$^+$ ILCs in the SILP are presented. All experiments were pooled from 2–3 separate experiments with 4–8 mice per group.

(D) Small intestinal gene expression of IL-4/IL-13 target genes *Ym1* (chitinase-like protein, CLP) and *Arg1* (arginase 1) in *Hpb*-infected Ifngr$^{+/+}$ and Ifngr$^{-/-}$ mice.

(E) Tuft and goblet cell enumeration in granuloma-associated regions of Ifngr$^{+/+}$ and Ifngr$^{-/-}$ mice following *Hpb* infection by immunofluorescence of double-cortin-like kinase (DCLK, tuft cells) and Lectin labeling (goblet cells), respectively. Quantification represents the average number of tuft or goblet cells per unit area of the crypt/villus axis surrounding the granuloma. Two pooled independent samples, n = 5–8 mice.

(F and G) (F) Enumeration of Gata3$^+$ IL13$^+$ CD4$^+$ T cells from the mesLNs and (G) quantification of the number and size of granulomas at 4 dpi following anti-IL-4 and anti-IL-13 treatment. Two pooled independent experiments, 6 mice per group. Each dot represents an individual mouse.

(H) Quantification of eYFP expression (IFNγ) by SILP CD4$^+$ T cells following *Hpb* infection at different time points. Representative contour plots pre-gated on CD45$^+$ TCRβ^+ CD4$^+$ T cells (left) and quantification (right) of frequency of eYFP$^+$ CD4$^+$ T cells of total CD4$^+$ T cells.

(I and J) (I) Representative contour plots of SILP IFNγ^+ CD8 T cells from uninfected or days 2 or 4 post-*Hpb* infection in WT mice following *ex vivo* PMA/ionomycin stimulation. Gated on live, CD45$^+$ TCRβ^+ CD8$^+$ T cells. Frequency and number of IFNγ^+ (J) CD8$^+$ T cells or CD4$^+$ T cells from the indicated time points following *Hpb* infection. Two independent experiments, n = 4–6 per group. Each dot represents an individual mouse. Between-group analysis was conducted with two-way ANOVA and Tukey's post hoc analysis. Time course analyses were conducted with two-way ANOVA and Tukey's post hoc analysis. *$p < 0.05$, **$p < 0.01$, ***$p < 0.001$; ns, not significant.

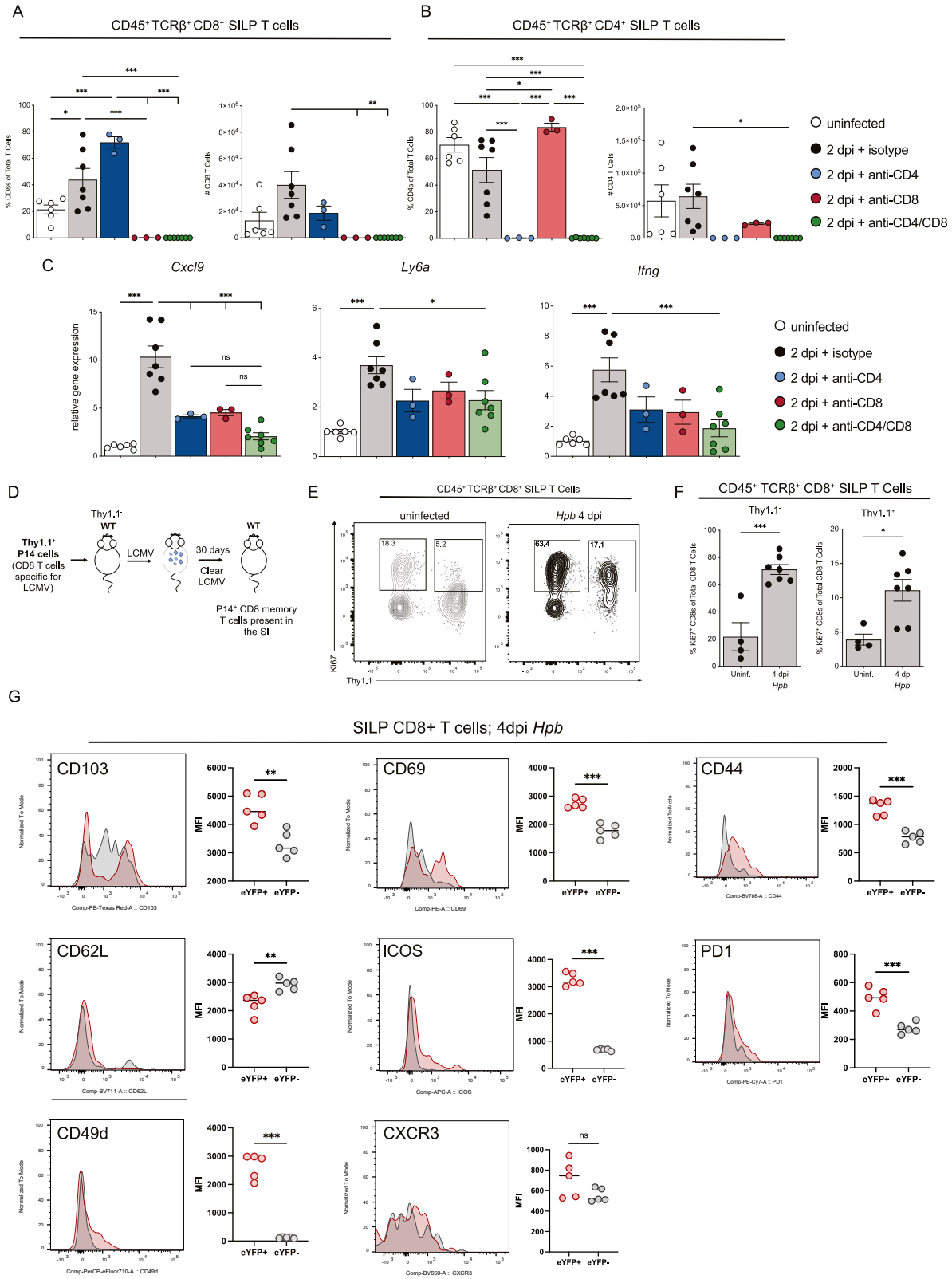

(legend on next page)

Figure S3. Characterizing T cell responses during early *Hpb* infection, related to Figure 2

(A–D) Depletion of $CD4^+$ T cells, $CD8^+$ T cells, or both was conducted with neutralizing antibodies. Quantification of (A) $CD8^+$ T cell frequency and number, (B) $CD4^+$ T cell frequency and number, and (C) ISG expression under all conditions is shown. Three independent pooled experiments, 3–8 mice per group. Each dot represents an individual mouse. To validate antigen-independent activation, an additional experimental approach was used (D) (see Figures 2H–2K). Purified LCMV-specific $Thy1.1^+$ P14 cells were adoptively transferred into $Thy1.1^-$ WT mice. Mice were infected with LCMV Armstrong. 30 days later, recipient mice were infected with *Hpb*.

(E) Representative contour plots of uninfected and day 4 *Hpb*-infected mice, gated on live, $CD45^+$ $TCR\beta^+$ $CD8^+$ SILP T cells.

(F) Quantification of $Ki67^+$ $CD8^+$ T cells of $Thy1.1^-$ (recipient) and $Thy1.1^+$ (donor P14) cells following *Hpb* infection at day 4. Two independent pooled experiments, $n = 4–8$ per group.

(G) $eYFP^+$ ($IFN\gamma$-producing) and $eYFP^-$ $CD8^+$ T cells were gated from live, $CD45^+$ $TCR\beta^+$ SILP cells at day 2 of *Hpb* infection, and the mean fluorescence intensity (MFI) of a selection of T cell activation and tissue-resident markers was assessed. Two independent pooled experiments, $n = 5$ mice per group. Each dot represents an individual mouse. Analyses were conducted with one-way ANOVA and Tukey's post hoc analysis, while between-group comparisons were analyzed with nonparametric Student's t test. $^*p < 0.05$, $^{***}p < 0.001$; ns, not significant.

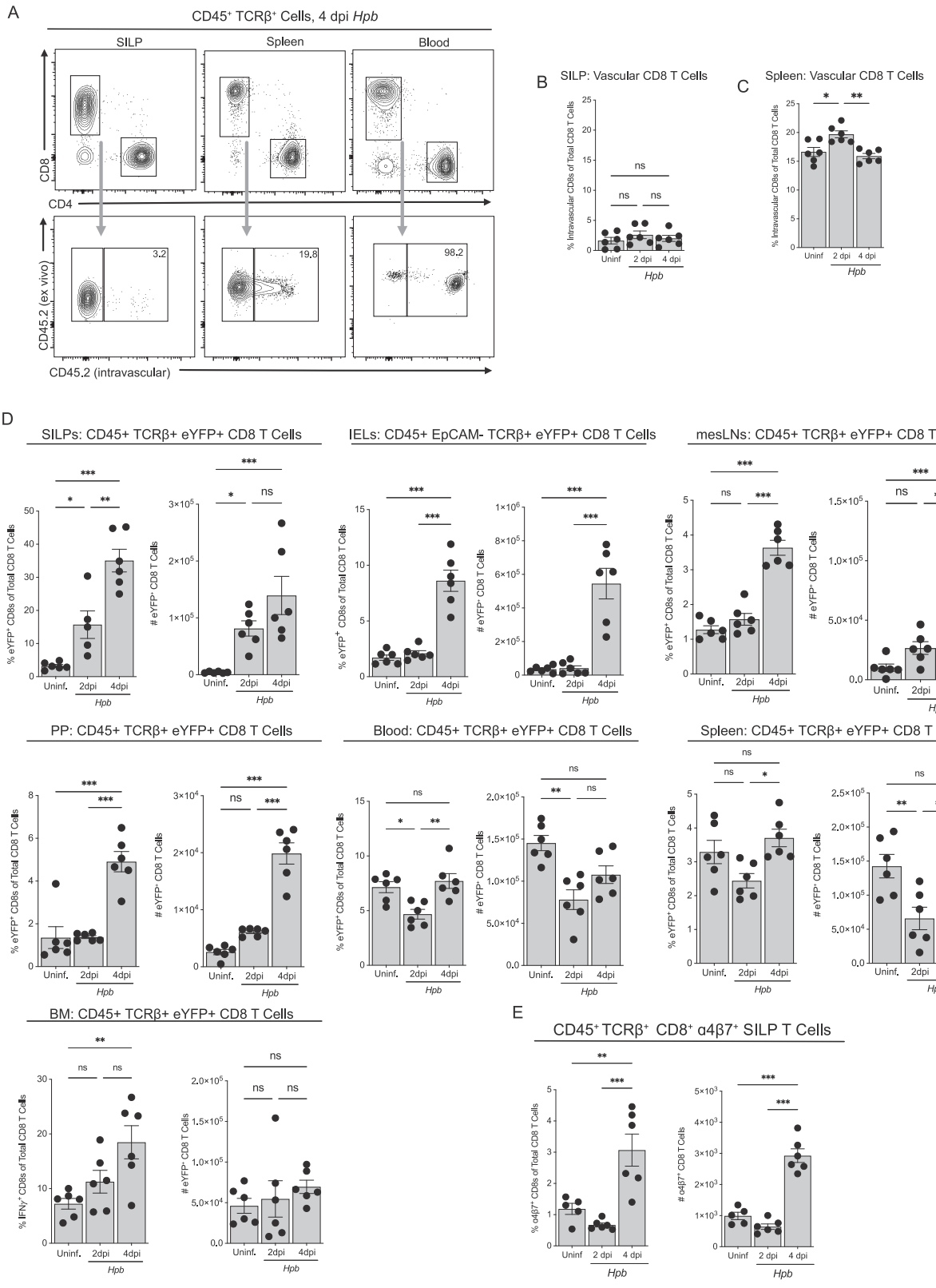

(legend on next page)

Figure S4. Systemic distribution of *Ifng*-expressing cells during early *Hpb* infection, related to Figure 2

(A) *Ex vivo* labeling was conducted by i.v. injection of color discordant CD45.2 antibodies, 3 min before sacrifice. Representative contour plots of viable T cells found in the SILP, spleen, or blood at 4 dpi are shown. Gated on live, total $CD45^+$ $TCR\beta^+$ T cells.

(B and C) (B) Quantification of the frequency of intravascularly labeled $CD8^+$ T cells within the SILP and (C) spleen, represented as a frequency of total $CD8^+$ T cells. Two independent pooled experiments, $n = 6$ per group. Each dot represents an individual mouse. Between-group comparisons were analyzed with nonparametric Student's t test.

(D) At days 2 and 4 post-*Hpb* infection, indicated tissues were harvested for enumeration of IFNγ-expressing ($eYFP^+$) $CD8^+$ T cells. In all cases, samples are gated on live, $CD45^+$ $TCR\beta^+$ $CD8^+$ T cells, and frequencies are represented as $eYFP^+$ cells as a percentage of total $CD8^+$ T cells. IELs, intestinal epithelial lymphocytes; mesLNs, mesenteric lymph nodes; BM, bone marrow; PP, Peyer's patches. Two independent pooled experiments, $n = 6$ mice per group.

(E) Quantification of the frequency and number of $\alpha4\beta7^+$ CD8 T cells in the SILP, from total $CD8^+$ T cells. Two pooled experiments, 6 mice per group. Each dot represents an individual mouse. Time course analyses were conducted with one-way ANOVA and Tukey's post hoc analysis. $^{**}p < 0.01$, $^{***}p < 0.001$; ns, not significant.

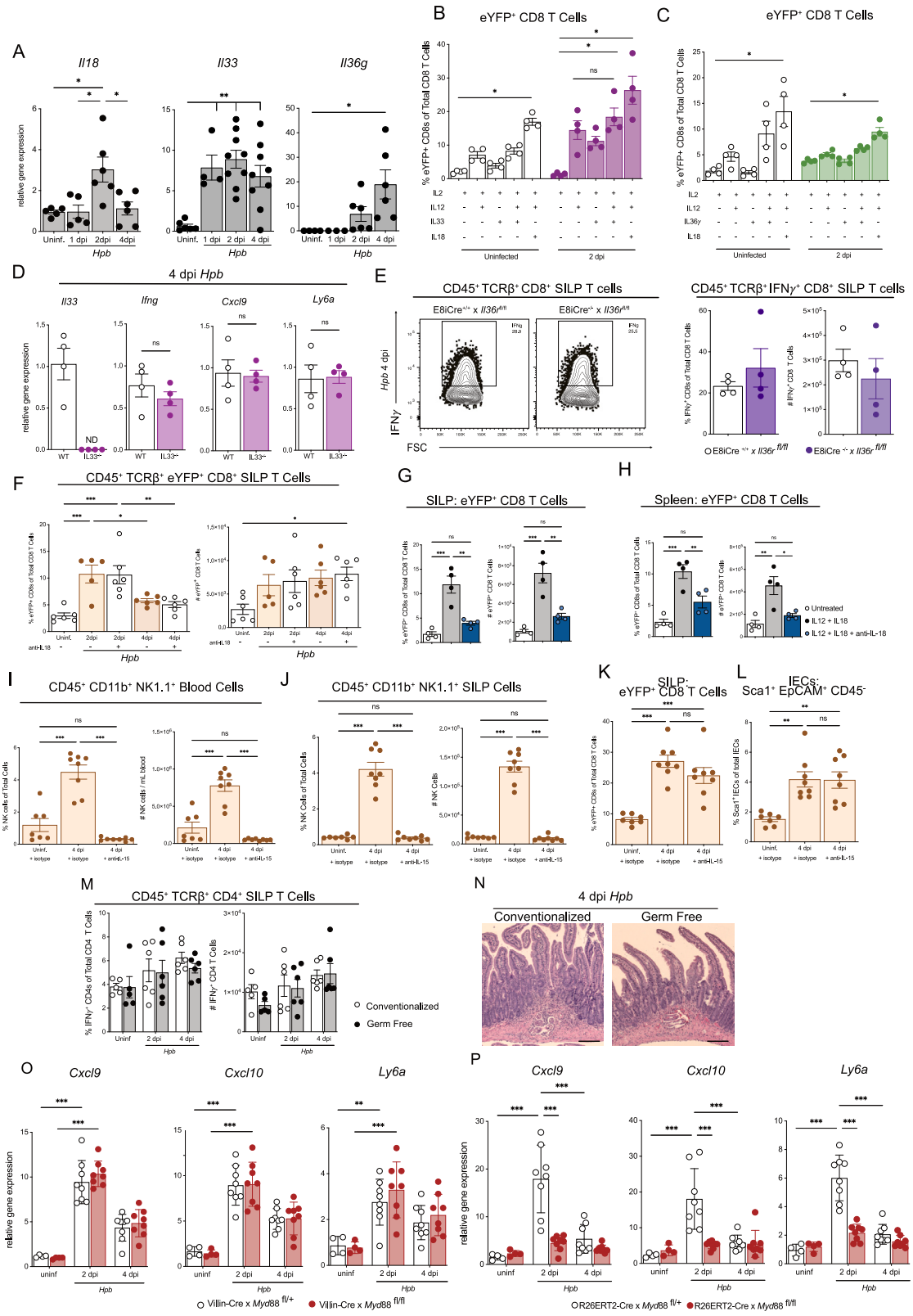

(legend on next page)

Figure S5. Role of alarmins in type 1 immunity during early *Hpb* infection, related to Figure 3

(A) *Il18*, *Il33*, and *Il36g* gene expression during early *Hpb* infection. Three independent pooled experiments, $n = 5–6$ per group.

(B and C) *In vitro* stimulation of SILP cells from uninfected and day 2 *Hpb*-infected eYFP$^+$ mice for 18h with the indicated combination of cytokines. Two independent experiments, $n = 4$ mice per group, with each dot representing a biological replicate.

(D) ISG expression analysis of day 2 *Hpb*-infected tissue from WT and Il33$^{-/-}$ mice. One experiment, $n = 4$ mice per group.

(E) Representative contour plots (right) and quantification (left) of IFNγ production by CD8$^+$ T cells from E8iCre$^{+/+}$ × *Il36r*$^{fl/fl}$ *Hpb*-infected mice stimulated *ex vivo* with PMA/ionomycin. Il36r is encoded by Il1rl2 gene, knocking out IL36α, β, and γ signaling. One experiment, 4 mice per group.

(F–L) (F) Frequency and cell count of eYFP$^+$ CD8$^+$ T cells at days 2 and 4 of *Hpb* infection, following administration of a neutralizing anti-IL-18 antibody. Two independent experiments, 5–7 mice per group. Validation of the anti-IL-18 blocking antibody following administration of recombinant IL-12 and IL-18 to mice. Quantification of eYFP$^+$ CD8$^+$ T cells in the (G) SILP and (H) spleen is shown, gated on viable, CD45$^+$, TCRβ$^+$ cells. One experiment, 4 mice per group. IL-15 activity was neutralized with an anti-IL-15 antibody and validated by NK cell quantification in the blood (I) and SILP (J). Quantification of (K) eYFP$^+$ CD8$^+$ T cells and (L) Sca1$^+$ epithelial cells in the SILP following treatment with anti-IL15 or isotype control. Two pooled independent experiments, 7–8 mice per group.

(M) Frequency and number of IFNγ^+ CD4$^+$ T cells in conventionalized and GF mice during *Hpb* infection. Gated on live, CD45$^+$ TCRβ$^+$ IFNγ^+ CD4$^+$ T cells.

(N) Representative H&E staining of conventionalized and GF mice at 4 days post-*Hpb* infection. Scale bar, 50 μm. One independent experiment, 3–4 mice per group.

(O) ISG expression in Villin-cre × MyD88$^{fl/fl}$ mice at days 2 and 4 post-*Hpb* infection compared with littermate controls.

(P) ISG expression in R26Ert2cre × MyD88$^{fl/fl}$ mice at days 2 and 4 post-*Hpb* infection compared with littermate controls. Two independent pooled experiments were performed for each genotype, 8 mice per group. Each dot represents an individual mouse. Time course analyses were conducted with two-way ANOVA and Tukey's post hoc analysis. Between-group comparisons were analyzed with nonparametric Student's t test and time course analysis with two-way ANOVA and Tukey's post hoc analysis. $^{**}p < 0.01$, $^{***}p < 0.001$; ns, not significant.

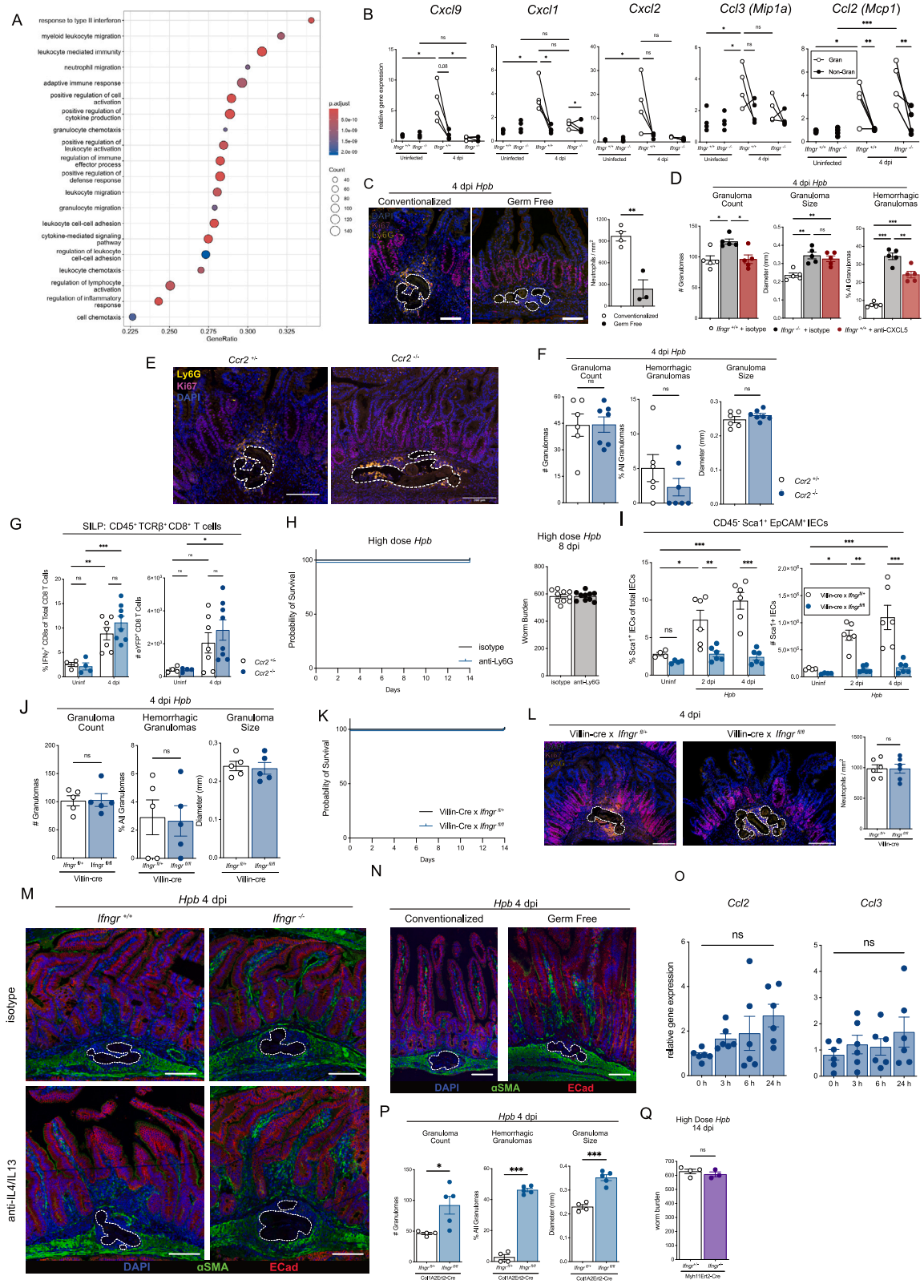

(legend on next page)

Figure S6. Cellular mechanisms of disease tolerance to *Hpb* infection, related to Figures 4 and 6

(A) Top 20 differentially expressed GO pathways at day 2 of *Hpb* infection compared with uninfected controls. Complete list of genes represented in Figure 4C of the main document.

(B) Gene expression analysis of various chemokines from tissue biopsies of granuloma- and non-granuloma-associated regions of *Hpb*-infected mice. One independent experiment, 4 mice per group. Line indicates paired granuloma and non-granuloma regions from the same mouse.

(C) Immunofluorescent staining (left) of neutrophils ($Ly6G^+$, yellow) in granuloma regions of conventionalized and germ-free mice at 4 days post-*Hpb* infection. Ki67, pink; DAPI, blue; scale bar, 50 μm (right). Total number of neutrophils per granuloma area (right). Each dot represents the average of 3–5 granulomas per mouse.

(D) Granuloma characterization of total number, size, and hemorrhagic scoring in $Ifngr^{+/+}$ mice treated with anti-Cxcl5 antibodies and controls. Two independent blinded experiments, 5–6 mice per group.

(E) Representative immunofluorescence images of neutrophil accumulation in granuloma regions in $Ccr2^{-/-}$ mice and littermate controls at day 4 post-*Hpb* infection. Ly6G, yellow; Ki67, pink; and DAPI, blue; scale bar, 200 μm.

(F) Characterization of granuloma-associated tissue remodeling in $Ccr2^{-/-}$ and control mice at day 4 of *Hpb* infection. Two independent pooled experiments, 6 mice per group.

(G) IFNγ production by $CD8^+$ T cells following *Hpb* infection isolated from the SILP of $Ccr2^{-/-}$ mice and littermate controls following *in vitro* PMA/ionomycin stimulation. Two independent pooled experiments, 4–8 mice per group.

(H) Survival plot (left) and worm burden (right) of high-dose infected mice treated with anti-Ly6G antibody from days −1 to 5 of *Hpb* infection. Two independent pooled experiments, 8–10 mice per group.

(I) Sca-1 expression by IECs in Villin-cre × $Ifngr^{fl/fl}$ mice and controls at days 2 and 4 of *Hpb* infection. Gated on live, $CD45^-$ $EpCAM^+$ cells. Two independent pooled experiments, 4–6 mice per group.

(J) Enumeration of granuloma counts, size, and hemorrhaging in Villin-cre × $Ifngr^{fl/fl}$ mice and littermate controls at day 4 of *Hpb* infection. Two independent pooled experiments, 5–6 mice per group. Investigator blinded to the experimental groups.

(K) Survival plot of high-dose (600 L3 larvae) infected Villin-cre × $Ifngr^{fl/fl}$ mice and control animals.

(L) Representative immune fluorescence imaging (left) and quantification (right) of neutrophil recruitment ($Ly6G^+$, yellow) in Villin-cre × $Ifngr^{fl/fl}$ mice and control animals at day 4 post-*Hpb* infection. Ki67, pink; DAPI, blue; scale bar, 100 μm. Two independent pooled experiments, 6 mice per group.

(M) Representative immunofluorescent imaging of αSMA remodeling in $Ifngr^{+/+}$ and $Ifngr^{-/-}$ mice following anti-IL-4 and anti-IL-13 treatment. DAPI, blue; αSMA, green; E-cadherin, red. Scale bar, 100 μm. Representative of two independent experiments, 4 mice per group.

(N) Representative immunofluorescent imaging of αSMA remodeling in conventionalized and germ-free mice at 4 dpi. DAPI, blue; αSMA, green; Ecadherin, red. Scale bar, 100 μm.

(O) QPCR analysis of chemokines of IFNγ-stimulated primary fibroblasts. Two independent pooled experiments, 6 mice per group.

(P) Quantification of granuloma counts, size, and hemorrhaging in Col1A2Ert2-cre × $Ifngr^{fl/fl}$ and Col1A2Ert2-cre × $Ifngr^{fl/+}$ mice at day 4 of *Hpb* infection. $n = 4–6$ mice per group.

(Q) Worm burden at 14 dpi in surviving high-dose infected Myh11Ert2-Cre × $Ifngr^{fl/+}$ or Myh11Ert2-Cre × $Ifngr^{fl/fl}$ mice. One experiment, $n = 3–5$ mice per group. Each dot represents an individual mouse. Between-group analyses were conducted with nonparametric Student's t test, time course with two-way ANOVA, and Tukey's post hoc analysis, while survival curves were analyzed with log-rank (Mantel-Cox) test. $^*p < 0.05$, $^{**}p < 0.01$, $^{***}p < 0.001$; ns, not significant.